Bachelor-Thesis
2010 - 03
March

The double-sided silicon strip detector with excellent position, energy and time resolution

Der doppelseitige Siliziumstreifendetektor mit exzellenter Positions-, Energie- und Zeitauflösung

Eleonora Teresia Gregor

(Bachelor-Thesis der TU Darmstadt)

GSI Helmholtzzentrum für Schwerionenforschung GmbH
Planckstraße 1 · D-64291 Darmstadt · Germany
Postfach 11 05 52 · D-64220 Darmstadt · Germany

The double-sided silicon strip detector with excellent position, energy and time resolution

Der doppelseitige Siliziumstreifendetektor mit exzellenter Positions-, Energie- und Zeitauflösung

Bachelor Thesis

Eleonora Teresia Gregor

14.12.09

Supervision:
Prof. Dr. Peter von Neumann-Cosel
Dr. habil Hans-Jürgen Wollersheim

ABSTRACT

In the scope of the RISING-project at GSI, a detector-array consisting of two rows of silicon-detectors was installed, with which excited states of highly exotic nuclei were investigated. The silicon detectors are used to stop the radioactive beam and at the same time allow for an energy measurement of the electrons, respectively positrons, resulting from the following β-decay. For this, an excellent position correlation between implantation and decay is required and for conversion electron spectroscopy a good energy resolution is needed.

In a second, similar setup, a part of the future PRESPEC-project, which is intended for isotopes with much shorter lifetimes, a silicon-detector shall also be used for the identification of such highly exotic nuclei. In this case, a start signal for a time-of-flight-measurement shall be given and an energy loss shall be measured.

This work describes the testing and calibration of the detectors intended for the active stopper, as well as tests with new preamplifiers, which shall allow for the simultaneous use of a silicon detector for time and energy measurements.

ZUSAMMENFASSUNG

Im Rahmen des RISING-Projekts an der GSI wurde ein Detektor-Array aus zwei Reihen Siliziumdetektoren aufgebaut mit dem angeregte Zustände von exotischen Kernen untersucht werden sollen. Die Siliziumdetektoren sollen den radioaktiven Strahl abstoppen und gleichzeitig eine Energiemessung der im nachfolgenden β-Zerfall entstehenden Elektronen beziehungsweise Positronen erlauben. Hierzu ist eine exzellente Positionskorrelation zwischen Implantation und Teilchenzerfall notwendig und eine gute Energieauflösung zur Messung der Konversionselektronen.

In einem zweiten, ähnlichen Aufbau, einem Teil des zukünftigen PRESPEC-Projekts, der für Isotope mit deutlich kürzerer Lebensdauer vorgesehen ist, soll ein Siliziumdetektor auch zur Identifikation eines solchen hochexotischen Kerns beitragen. In diesem Fall soll er ein Start-Signal für eine Flugzeitmessung liefern und außerdem einen Energieverlust messen.

Diese Arbeit beschreibt das Testen und Kalibrieren der Detektoren, die für das erste Experiment verwendet wurden, sowie Tests mit neuen Vorverstärkern, welche die gleichzeitige Benutzung des Siliziumdetektors zur Zeit- und Energiemessung ermöglichen sollen.

CONTENTS

1. Introduction 8

2. Semiconductor Diode Detectors 10
2.1 Semiconductor properties 10
2.2 Semiconductors as ionisation detectors 11
2.3 Operational characteristics 12
2.4 Microstrip detectors 13

3. Energy measurement with a double-sided silicon strip detector 14
3.1 The double-sided silicon strip detectors (DSSSD) 14
3.2 The electronics for the active stopper 15
3.3 Testing the active stopper with a ^{207}Bi-source 16
3.4 Energy calibration and resolution with a mixed α-source 17

4. Time measurement with a DSSSD 19
4.1 The microchannel plate detector (MCP) 19
4.2 The setup for the UNILAC-experiment 20
4.3 Time measurement with two microchannel plate detectors 20
4.4 Time resolution between MCP and DSSSD using the new GSI preamplifier 22
4.4.1 Estimating the best possible time resolution 22
4.4.2 Results from the time measurement 24
4.5 Testing the Mesytec MFA-32 26

5. Summary and Outlook 28

Appendix 29

A. Detailed results for the active stopper detectors 2524-21, 2536-3, 2524-24, 2540-21, 2512-17, 2243-3 30

B. Exemplary results for time strip 7 39

C. Technical details of the preamplifiers 40

LIST OF FIGURES

2.1 The bonds around the two kinds of impurities; donor (left) and acceptor (right). The arrows show the extra electron and the unsaturated bond, respectively. [Kra05] 11
2.2 The schematics of a double-sided silicon strip detector with a particle of ionising radiation creating charge carriers along the track. [Kra05] 13

3.1 Schematic drawing provided by Micron Semiconductor Ltd. [Micron] 14
3.2 Photo of a W1(DS)-1000 detector in the vacuum vessel together with the ^{207}Bi-source. 14
3.3 Output signal from the preamplifier MPR-32 for a measurement with a ^{207}Bi-source 15
3.4 Output signal from the STM-16 shaper for a measurement with a ^{207}Bi-source . . 15
3.5 Block diagram of the electronics setup with a DSSSD, one MPR-32 preamplifier, two STM-16 shaper and discriminator modules, a VME-powered CAEN V785 ADC and the data taking computer 16
3.6 Energy spectrum from strip X9 of detector 2524-21 for the ^{207}Bi conversion electron source 17
3.7 Energy resolution in keV plotted over strip number for detector 2524-21 measured with a ^{207}Bi conversion electron source 17
3.8 The active stopper box in the RISING-setup 18
3.9 Energy spectrum from front strip X3 for the mixed α-source 18
3.10 Energy resolution in keV plotted over strip number measured with the mixed α-source 18

4.1 Photo of one of the MCP detectors used in this experiment. 19
4.2 Technical drawing of a MCP detector. [Kon08] 19
4.3 The block diagram for the UNILAC experiment with an energy branch, consisting of a MPR-32 preamplifier, a STM-16 shaper and a V785 ADC, and a time branch, consisting of two different amplifiers and CFDDs and a V1290A multihit-TDC . . 20
4.4 Time spectrum between the two MCPs with a gate on pixel 7 (time branch):8 (energy branch) of the DSSSD 21
4.5 The DSSSD mounted on the new preamplifier. 22
4.6 A typical signal from strip 8 (dark blue) of the preamplifier. Note the well visible smaller signal in strip 7 (light blue); a cross-talk signal. 23
4.7 Magnification of a signal from strip 2. Risetime can be estimated as 600 ps in an interval of 20 mV 23
4.8 The time-of-flight between MCP 1 and time strip 7 of the DSSSD without the gate on a pixel. The unit of the x-axis is channels; each channel corresponds to 25 ps. The five time peaks can be assigned to the energy strips 0 & 1, 2 & 3, 4 & 5, 6 & 7 and 8, 9, 10 & 11, respectively. 24
4.9 The time of flight between MCP 1 and time strip 7, energy strip 2 of the DSSSD . 25
4.10 The signal from the MPR-32 (1, yellow) and the MFA-32 (2, blue) obtained with a ^{241}Am-source 26
4.11 Energy signal in channel 1 (dark blue), time signal in channel 2 (light blue) 27

4.12 Energy signal in channel 1 (dark blue), time signal in channel 2 (light blue). The risetime of the timing signal is approximately 100 ns. 27

A.1 Energy resolution versus strip number for detector 2524-21 31
A.2 Energy resolution versus strip number for detector 2536-3 31
A.3 Energy resolution versus strip number for detector 2524-24 34
A.4 Energy resolution versus strip number for detector 2540-21 34
A.5 Energy resolution versus strip number for detector 2512-17 37
A.6 Energy resolution versus strip number for detector 2243-3 37

B.1 Time resolution versus energy strip number in time strip 7 39

C.1 The detailed layout of one strip of the GSI preamplifier, provided by Wolfang König 40
C.2 The layout of the top side of the GSI preamplifier, provided by Wolfang König . . 42
C.3 The layout of the bottom side of the GSI preamplifier, provided by Wolfang König 42

LIST OF TABLES

4.1 shows the strip number, slope of the pulse ΔV and estimated time resolution . . . 24

A.1 Detailed results for detector 2524-21 30
A.2 Detailed results for detector 2536-3 32
A.3 Detailed results for detector 2524-24 33
A.4 Detailed results for detector 2540-21 35
A.5 Detailed results for detector 2512-17 36
A.6 Detailed results for detector 2243-3 38

B.1 Detailed results for time strip 7 (all numbers in ps). The first four columns are the fit parameters from the spectra; the next four the two calculated time resolutions with their errors; the last column shows the weighted mean for each strip. 39

1. INTRODUCTION

The study of the internal structure of exotic atomic nuclei has become a main interest in nuclear physics research. The RISING (Rare Isotope Spectroscopic INvestigation at GSI) project, which combines the GSI's FRS (FRagment Separator) [Gei92] and the EUROBALL [Sim97] cluster detectors, has two main interests in this field: the shell-structure of neutron-rich nuclei and the isospin symmetry in proton-rich nuclei. Two main setups will be used; one for decay- [Pie07] the other for scattering experiments [Wol05].

Particle fragmentation is used to produce exotic ion beams at relativistic energies. During this peripherical reaction angular momentum is transferred and the fragments are excited. The secondary beam is then analysed by the FRS, where the nuclei of interest are separated from the unwanted ones. In the resulting beam, each nucleus has to be identified uniquely. This is done via time-of-flight measurements with two plastic detectors, the Bρ settings of the FRS magnets and energy loss in an ionisation chamber (MUSIC); in addition multiwire-detectors are used to track the flight path.

For decay experiments, the nuclei are then implanted in an array of silicon detectors, the so-called active stopper [Kum09]. This array consists of six silicon detectors arranged in two rows of three and surrounded by the 15 EUROBALL germanium detectors. Silicon detectors can be run both in vacuum and in air; since vacuum would require a thick steal chamber with an entrance window, which would partially absorb both the beam and the gamma-rays, they are operated at atmospheric pressure. Since air moisture can have damaging effects on a running detector, the experiment is performed in dry nitrogen and the detectors can be kept in a thin-walled chamber. After the implantation, the excited states of the nucleus will decay, emitting gamma-rays of isomers. The implanted radioactive nucleus will undergo a beta-decay after milliseconds or seconds, emitting an electron or positron and simultaneously one or more gamma-rays. It can be ascertained that both events come from the same implanted ion, if their point of origin is the same. The first part of this work is to test detectors for this active stopper.

The setup described above makes it impossible to study excited states with lifetimes shorter than 200 ns, which is the approximate time-of-flight of an ion through the FRS. For scattering experiments, the secondary beam from the FRS is impinged on a secondary target. The goal is to produce excited nuclei. The short-lived states of interest decay directly after the target and the gamma-rays are again seen in the EUROBALL detectors. However, scattering at a target can also cause other, unwanted reactions, which change the element and mass number of the scattered fragment. Therefore the resulting particles have to be identified again. This is done in a similar way as before the target, via energy loss and time-of-flight. Just after the target, one or two detectors measure the position and give the start signal for the ejectile. Almost four metres downstream a ΔE-E telescope of the LYCCA (Lund-York-Cologne-CAlorimeter) [Rud08] array, consisting of a position sensitive silicon detector and a caesiumiodide detector, is installed, which measures the residual energy of the ejectile fragment. In front of LYCCA, a plastic detector is installed to give the stop signal for the time-of-flight-measurement. A time-of-flight measurement allows the calculation of the mass since the energy $E_{kin} = mc^2(\gamma - 1)$ is also known; the energy loss ΔE is proportional to Z^2. Both informations are sufficient to identify the nucleus once more. [Pod08]

Since the particles used in this experiment are highly exotic nuclei, the count rate is rather

low; also the half life of the nuclei is rather short and a number of them may already decay before reaching the last detector. Therefore, the large number of detectors used just for the identification of the nuclei can be problematic. It is therefore the aim of this work to investigate whether it might be possible to use just one detector for energy loss, time and position measurements close to the target position.

The theoretical idea is the following: It is impossible to get both a good energy resolution and a good time resolution from the same signal. Energy resolution requires a long integration over a signal to include as much of the deposited energy as possible. Time resolution, however, requires a short integration to get a fast pulse with a clearly defined beginning. If a double-sided strip detector is used, the signals from one side could be integrated to get the energy loss, while the other could yield a start signal for a time measurement. The stop signal would be given by the plastic detector in front of the LYCCA array.

In the following, the properties of semiconductor diode detectors will be described. Chapter 3 summarizes the results of the energy measurements with a double sided silicon strip detector. The time measurements with the same detectors are explained in chpater 4 and the results are discussed. A summary of this thesis is given in chapter 5.

2. SEMICONDUCTOR DIODE DETECTORS

2.1 Semiconductor properties

The important energy bands for explaining conductivity are the valence band and the conduction band. In the valence band, electrons are bound to specific lattice sites within the solid; electrons in the conduction band can migrate freely through the solid. The main difference between metals, semiconductors and insulators is the size of the bandgap between those two bands. In a metal, the bandgap is zero, or the two bands may even overlap. For insulators, the bandgap is usually 5 eV or more, whereas semiconductors have considerably smaller bandgaps (1.115 eV for silicon at room temperature).

At any non-zero temperature, some thermal energy is shared by the electrons in the solid. It is possible for an electron in the valence band to gain sufficient energy to be elevated across the bandgap to the conductivity band, leaving behind a vacancy called a hole. The probability of thermal excitation p(T) is a strong function of the temperature T and the bandgap E_g [Kno00]:

$$p(T) = CT^{\frac{2}{3}} \exp -\frac{E_g}{2kT} \tag{2.1}$$

Electrons can move relatively freely through the conduction band; a hole moves from one position to another if an electron leaves that position to fill the existing vacancy. A mobility for both electrons and holes can be defined as the fraction of the electric field magnitude and the drift velocity. The mobilities of electrons and holes are roughly of the same magnitude. Therefore both charge carriers contribute to the electrical current, which is part of the reason for the higher energy resolution of semiconductor detectors.

A perfectly pure semiconductor is called intrinsic; the number of electrons or holes obtained at the equilibrium of thermal excitation and subsequent recombination are known as the intrinsic carrier densities. However, the advantages of small concentrations of impurities lead to the use of doped semiconductors.

Most semiconductor materials, especially silicon and germanium, are tetravalent. In crystal lattices, each atom forms covalent bonds with the four nearest atoms. In an intrinsic material, excitation of an electron leaves behind an unsaturated bond. To dope the semiconductor, small concentrations of impurities are added. Let us first assume a pentavalent impurity. If the concentration is sufficiently small (a few parts per million or less), the impurity atoms occupy substitutional sites within the lattice. Since it can only form four covalent bonds with the nearest atoms, one electron is left over (see figure 2.1). This extra electron remains only very lightly bound to the impurity site and can occupy an energy level within the normally forbidden bandgap, close to the bottom of the conductivity band. It therefore takes only very little energy to elevate it up into the conduction band without leaving a hole behind. Impurities of this kind are called donor impurities; the material is known as n-type semiconductor.

A p-type semiconductor can be obtained by adding trivalent impurities to the lattice. If the impurity occupies a substitutional site, it has one valence electron left and one of the covalent bonds is left unsaturated (see figure 2.1). This creates a vacancy similar to a hole. An electron can be captured to fill this vacancy and saturate the bond. Additional electron sites within the normally

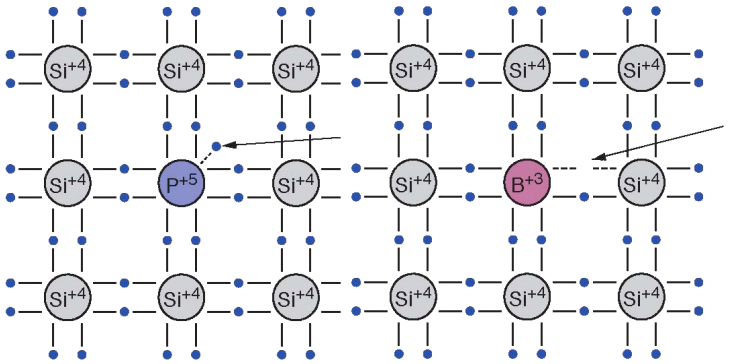

Fig. 2.1: The bonds around the two kinds of impurities; donor (left) and acceptor (right). The arrows show the extra electron and the unsaturated bond, respectively. [Kra05]

forbidden bandgap are again created which lie close to the top of the valence band. Impurities of this kind are known as acceptor impurities.

For both types it can be said that a charge carrier is created for each impurity that is added. Thus, the normal equilibrium between holes and electrons is shifted towards the majority carriers; the product of the numbers of excited electrons and holes must stay the same. From this follows that the conductivity of a doped semiconductor will always be higher than that of the intrinsic material. ´

2.2 Semiconductors as ionisation detectors

When any kind of ionising radiation passes through a semiconductor, it will create electron-hole pairs along the track (see figure 2.2). There is an average energy needed to produce one electron-hole pair, the ionisation energy. Semiconductor detectors have a very small ionisation energy of 3,62 eV for silicon [Kno00] at room-temperature compared to approximately 30 eV in a typical gas-filled detector. The number of charge carriers is therefore about ten times higher, which increases the energy resolution as the statistical fluctuation of charge carriers becomes a smaller fraction of the total as the amount of charge carriers is increased.

Electrons and holes created in a semiconductor tend to migrate until recombination takes place. Observed lifetimes are in the order of microseconds, due to the residual impurities present. Some of these impurities, mostly metallic atoms that occupy substitutional lattice positions, introduce additional electron sites in the middle of the forbidden gap, called deep impurities. They can act as so-called traps, in the sense that they may capture a charge carrier which is immobilised for a relatively long period of time. Although it may eventually be released, the delay will prevent it from contributing to a measured pulse. Deep impurities may also act as recombination centres. Such an impurity near the middle of the bandgap may capture an electron and shortly afterwards a hole, causing the two to recombine. This kind of recombination is far more common than direct recombination across the full bandgap. It is sufficient for the average lifetime to be two to three orders of magnitude shorter than the collection time.

Most semiconductor detectors are based on the favourable properties created near the junction between n- and p-type semiconductor materials. Junctions are created within a single crystal, normally by exposing it to a vapour of the required impurity which then diffuses some distance into the crystal. In the n-type material the density of conduction electrons will be much higher than in the p-type material. Therefore, a strong gradient exists at the junction and a net diffusion

from regions of high concentration to low concentration must take place. Conduction electrons will therefore migrate into the p-type material, where they will quickly recombine with holes. An equivalent argument leads to the conclusion that holes also migrate into the n-type material. The combined effect is to build up a negative charge on the p-side and a positive charge on the n-side, creating a region in which less or no charge carriers exist, the depletion region. It extends into both p- and n-sides of the junction; the distances depend on the concentrations of impurities. If the concentration of donor impurities in the n-side is higher than the concentration of acceptor impurities in the p-side, then the electrons migrating across the junction will travel a greater distance before they all have recombined with holes and the depletion region will extend farther into the p-side.

An electric field in the depletion region causes all electrons or holes created near the junction to be swept back to one side. The only remaining charges are the ionised donor sites and filled acceptor sites which are immobilised and therefore do not contribute to conductivity. The depletion region shows a high resistivity. If ionising radiation passes through the depleted region, the created electrons and holes will be swept out of the region quickly and their motion constitutes a basic electrical signal.

A junction functions at the same time as a diode. If an external bias voltage is applied in forward direction (a positive voltage to the p-side), the potential will attract conduction electrons across the junction to the p-side and holes to the n-side. Since these are the majority carriers, conductivity through the junction is greatly enhanced. However, if an external voltage is applied in backwards direction, so-called reverse biasing, (a negative voltage to the p-side), the potential difference which already exists between the two regions is enhanced. The minority carriers are attracted across the junction; conductivity and resulting current are quite small. Because of the growing potential difference, Poisson's equation demands an increase of the space charge and a further extension of the depletion region into each side, increasing also the volume in which charge carriers are collected.

2.3 Operational characteristics

Most detectors are operated with sufficient reverse bias voltage so that the depletion region extends through the entire wafer of the detector. This is a fully or totally depleted detector. The full depletion voltage can be theoretically calculated as [Kno00]:

$$V_d = \frac{eNd^2}{2\varepsilon} \tag{2.2}$$

d is in this case the wafer thickness, N the number of charge carriers and ε the dielectric constant (12 for silicon). If the reverse bias is further increased, the electric field will also increase and the detector is now called overdepleted. Further increasing will cause a sudden breakdown in the diode; the reverse current will abruptly increase, often with destructive effects. It is therefore important to keep the depletion voltage is low as possible. To obtain this result, one side of the junction is often made of heavily doped material, while the opposite side is only very mildly doped. This side will be the thicker one, since the depletion region automatically extends farther into this side; while the heavily doped layer can be very thin.

Fully depleted detectors have several advantages over partially depleted detectors. A partially depleted detector has a region without an electric field, in which the charge carrier velocities are strongly reduced. This increases the collection time so that the risk of carrier loss also becomes larger, which degrades the energy resolution. The rise of the signal pulse is also slowed down, degrading the timing properties.

When a reverse bias voltage is applied to a junction detector, a small current in order of a few hundred nanoamperes is normally observed. This is called the leakage current. Bulk leakage

currents are caused by two mechanisms: First, there is the free migration of the minority carriers over the junction, which only causes a small current. The second cause is the so-called generation current, which is caused by thermal excitation and can only be reduced by cooling. Surface leakage takes place at the edges of the junction. The amount varies greatly and depends on factors such as detector encapsulation, humidity and contamination of the surface.

Leakage current should always be monitored closely since abrupt changes indicate a change in the detector performance. Any use of a detector ensures that some damage to the lattice will take place because of the effects of the radiation passing through the crystal. The creation of electron-hole pairs is fully reversible, but the transfer of non-ionising energy to the atoms of the crystal can lead to irreversible damage. Those effects increase with the mass of the particle. The major type of damage is the so-called point defect, which is produced by the displacement of one atom from its normal lattice site due to energy transfer from the incoming radiation. Complex clusters of damage in the lattice can be formed if sufficient energy is transferred. Since these defects can trap charges and cause recombination, they degrade the energy resolution of the detector.

2.4 Microstrip detectors

One of many possibilities to create a position-sensitive detector is to subdivide the electrode into a number of independent segments. Electron-hole pairs created in the volume of the detector will travel along the field lines, so that a strong signal will only be derived from the corresponding electrode segment. Double-sided Microstrip detectors are mostly produced in configurations similar to figure 2.2. Since the motions of electrons and holes will induce charges on either side of the

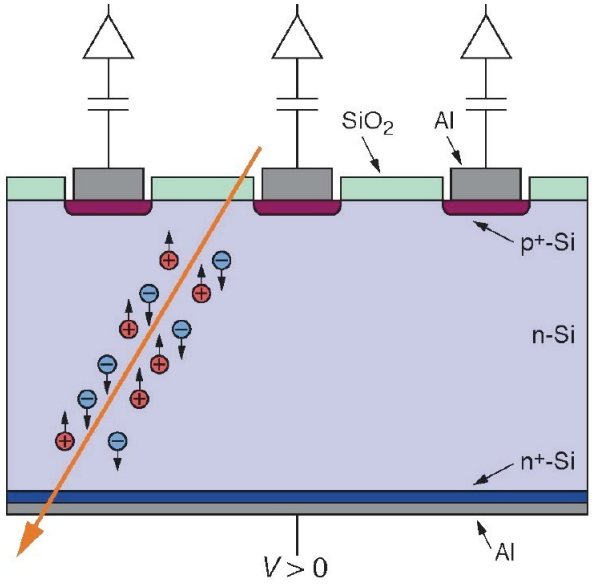

Fig. 2.2: The schematics of a double-sided silicon strip detector with a particle of ionising radiation creating charge carriers along the track. [Kra05]

detector, x- and y-coordinates are obtained for each event. Usually, more than one strip is activated, so that a distribution can be analysed which results in a position resolution better than the strip width.

3. ENERGY MEASUREMENT WITH A DOUBLE-SIDED SILICON STRIP DETECTOR

3.1 The double-sided silicon strip detectors (DSSSD)

The used detector model was the W1(DS)-1000 detector from Micron Semiconductor Ltd. [Micron] (see figure 3.1). 16 strips on both sides provide 265 3x3 mm^2 pixels on the active area of 5x5 cm^2. Full depletion is normally obtained at 180-200 V, but some detectors have to be run at higher bias voltages, especially if they have been used in prior experiments. The second model used, W1(DS)-40 is similar to the first, with the difference that the detector is only 40 μm instead of 1000 μm thick. A bias voltage of 10 V is sufficient for full depletion. Both detectors were mounted on a special adaptor designed by Mesytec [Mes] and connected to the preamplifier via two twenty pole flat ribbon connectors. Figure 3.2 shows the W1(DS)-1000 detector in a vacuum vessel during the energy measurement.

Fig. 3.1: Schematic drawing provided by Micron Semiconductor Ltd. [Micron]

Fig. 3.2: Photo of a W1(DS)-1000 detector in the vacuum vessel together with the ^{207}Bi-source.

3.2 The electronics for the active stopper

The Mesytec MPR-32 preamplifier [MPR32] is a 32-channel preamplifier, so that it can be used for both the 16 front and 16 back strips of a single double-sided strip detector. It can accept both positive and negative input polarities and amplifies them equally. The input connectors are subD 25 female connectors; the output are twisted pair 34 male header connectors. The MPR-32 exists in linear and logarithmic mode, but in the present experiments only linear mode was used. Amplification ranges of 5 or 25 MeV can be chosen. The full output range is 4 V.

A typical output signal of the preamplifier is shown in figure 3.3. The signal height is about 250 mV; the decay time roughly 35 μs. The signal-to-noise-ratio is about 10:1.

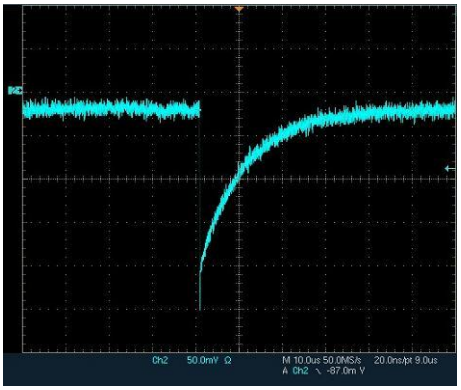

Fig. 3.3: Output signal from the preamplifier MPR-32 for a measurement with a ^{207}Bi-source

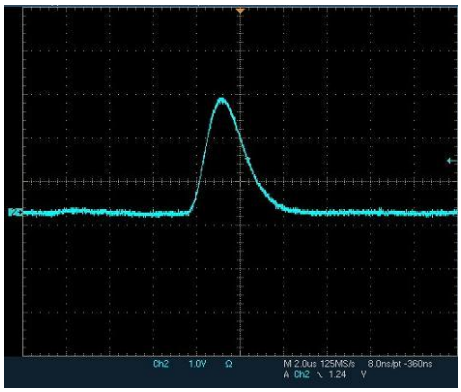

Fig. 3.4: Output signal from the STM-16 shaper for a measurement with a ^{207}Bi-source

The high-voltage for the detector is supplied by a MHV-4 module [MHV4], which is connected to the preamplifier via LEMO 00 cables. The outputs of the MPR-32 were connected to two NIM-powered Mesytec STM-16 shaping/timing filter/discriminator modules [STM16]. Two versions of this module exist; the differential input version, which was used here, has 16 channels, so that two units are needed for a single DSSSD. Both in- and output connectors are twisted pair 34 male header connectors. The gain can be adjusted in 16 steps with a factor of 1.22 per step; the threshold in 256 steps; the maximum threshold is equal to 40% of the maximum output range, which is 10 V. A shaping time of 1 or 2.5 μs (FWHM) can be selected by a jumper inside the case and is common for all channels. The polarity can be changed with a 4·16 pole connector inside the case. An output signal is shown in figure 3.4.

The STM-16 can be controlled by a NIM-module MRC-1 [MRC1], which can monitor up to 32 Mesytec modules. Via the MRC-1, both gains (for pairs of channels) and thresholds (for each individual channel) can be remotely controlled. Communication with a control PC is done via RS-232 serial interface; the connection to the STM-16-modules via LEMO 00 coaxial cables. The analogue output signals of the STM-16 shaper were fed directly into a CAEN V785AF ADC [ADC] (analogue-to-digital-converter). The input connectors are two 34 pin male connectors; the maximum input voltage is 8 V. The trigger from the STM-16 is a logical OR of the triggers from all 16 discriminator channels and was used to produce both the trigger for the data taking CES RIO3 8064 [RIO], a VME-powered CPU, and the ADC gate. Figure 3.5 shows a detailed block diagram of the electronics setup.

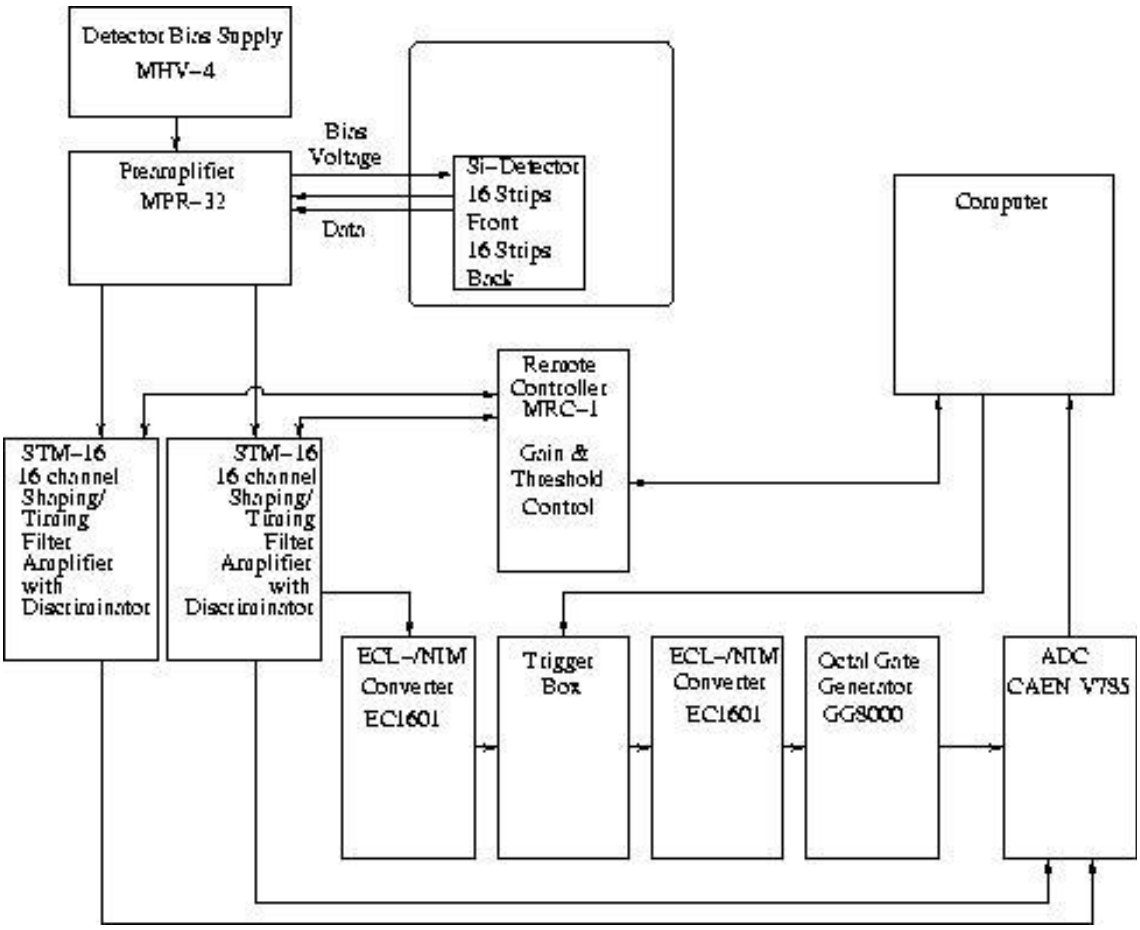

Fig. 3.5: Block diagram of the electronics setup with a DSSSD, one MPR-32 preamplifier, two STM-16 shaper and discriminator modules, a VME-powered CAEN V785 ADC and the data taking computer

3.3 Testing the active stopper with a ^{207}Bi-source

The testing of the six DSSSDs working as an active stopper in the decay experiments was done with a ^{207}Bi conversion electron source. The data were used for energy calibration. One measurement was first performed with a DSSSD to determine whether a long or a short shaping time should be used. For the energy measurements, the data acquisition programme Go4 [GO4] was used, a GSI analysis system based on ROOT. The analysis was also performed in Go4. For the time measurements, ROOT [ROOT] itself was used for the analysis.

For short shaping time (1 μs FWHM), the mean energy resolution was 1.96% for the front and 2.05% for the back side, whereas for long shaping time (2.5 μs FWHM), mean energy resolutions of 1.83% (front) and 1.86% (back) could be reached. Therefore, a shaping time of 2.5 μs (FWHM) was used for all other test measurements. The gain was set to 10, which equals a gain factor of 12.2. Amplifier thresholds were set just above the noise level with the help of an oscilloscope to values between 29 and 54.

The measured electron spectrum in figure 3.6 was obtained for the strip X9 of detector 2524-21.

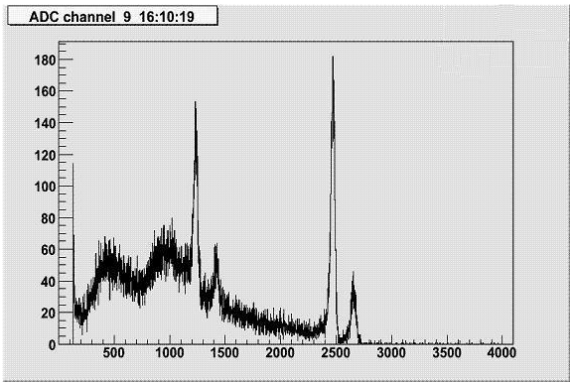

Fig. 3.6: Energy spectrum from strip X9 of detector 2524-21 for the ^{207}Bi conversion electron source

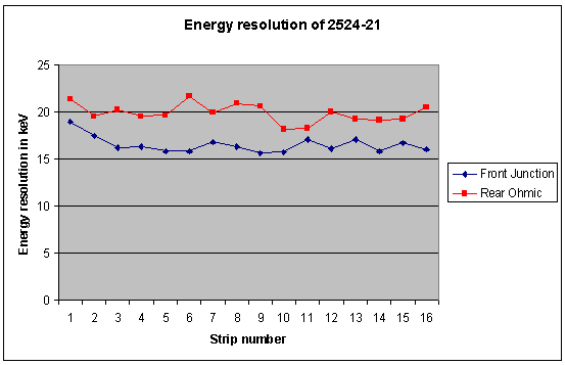

Fig. 3.7: Energy resolution in keV plotted over strip number for detector 2524-21 measured with a ^{207}Bi conversion electron source

Four peaks can be clearly seen, which are due to K and L/M conversion of the 570 keV and 1064 keV transition in ^{207}Pb. The K-conversion peaks lie at 482 keV and 976 keV, the L- and M-conversion peaks at 554-567 keV and 1048-1061 keV respectively. The latter are so close in energy that they cannot be resolved into two separate peaks. The K-conversion peaks, which have clearly defined energies were then used to calibrate the detectors; the energy resolution was always determined for the 976 keV peak. Typical energy resolutions for front junction sides were around 15 keV to 19 keV, and in the region of 18 keV to 21 keV for rear ohmic sides. Detailed results of all six DSSSDs can be found in the appendix. Figure 3.7 shows an overview of the energy resolution versus the strip number for detector 2524-21. It can be clearly seen that the resolution of the front junction side is better than that of the rear ohmic side. The energy resolution is somewhat poorer for edge strips. Detailed results for all six detectors can be found in appendix A.

Seven detectors were tested; one of them was already replaced after some preliminary measurements, due to its high leakage current and resulting poor energy resolution.

After testing all DSSSDs, six of them were mounted in the active stopper vessel made out of pertinax (phenolic-formaldehyde cellulose-paper PF CP 2061) with an entrance and exit window covered by a 20 μm thin black pocalon carbon foil. The pertinax wall was 2 mm thick. For the RISING decay experiments the logarithmic MPR-32 multi-channel preamplififer was used. It provides a linear range of 2.5 or 10 MeV, which covers 70 % of the total range. The last 30 % cover the energy range from 2.5 or 10 MeV respectively to 3 GeV. In this way, both the fast fragment implantation and the emitted β-particles can be measured. I implemented the active stopper (see figure 3.8) in the RISING setup and was responsible for it during the experiments S337, S350 and S361 in September 2009.

3.4 Energy calibration and resolution with a mixed α-source

Before the thin W1-DS(40) detector was used in the UNILAC accelerator experiment at cave X7, the energy resolution was determined. Measurements were performed with the DSSSD inside a vacuum vessel (see figure 3.2) with a mixed source (^{241}Am, ^{239}Pu and ^{244}Cm) positioned at a distance of about three cm from its surface. Energy calibration was done via all three resulting peaks at 5.245 MeV (Pu), 5.476 MeV (Am) and 5.902 MeV (Cm). The 5.486 MeV peak from the Americium was also used for determining the energy resolution. The range of 5 MeV α-particles

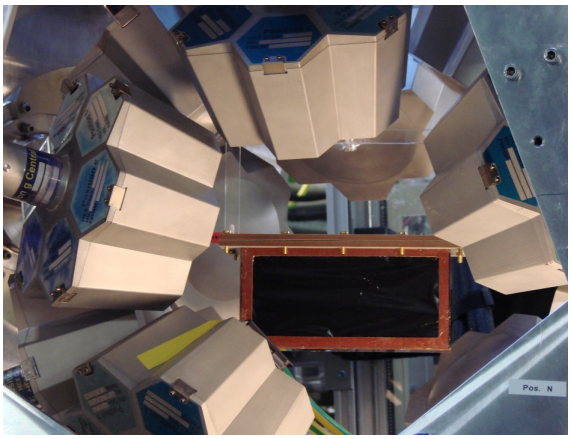

Fig. 3.8: The active stopper box in the RISING-setup

in silicon is approximately 28 μm; they should therefore be completely stopped even in the thin 40 μm detector. The same electronics as for the active stopper were used. Figure 3.9 shows a typical energy spectrum.

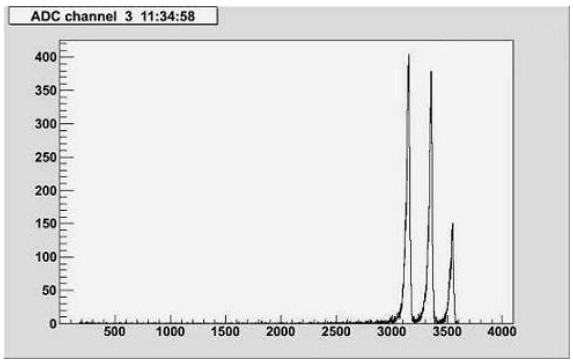

Fig. 3.9: Energy spectrum from front strip X3 for the mixed α-source

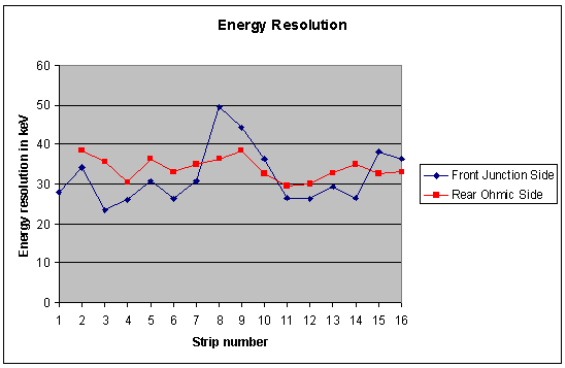

Fig. 3.10: Energy resolution in keV plotted over strip number measured with the mixed α-source

Energy resolutions of 0.61%-0.98% could be reached for front strips; 0.8%-1.03% for back strips. Two front strips displayed an energy resolution of more than one percent, which is probably due to the prior use of the detector for measuring heavy ions and some slight resulting damage. Edge strips generally showed a somewhat poorer energy resolution. The resolution for the front junction side was in most cases better than that of the rear ohmic side, except for three possibly slightly faulty strips. Figure 3.10 shows an overview of the energy resolution of each strip. There were no data from strip Y1, as this strip has been damaged in a prior experiment. Its leakage current was so high that the alphas could not be seen above the noise. However, one badly damaged strip and an edge strip at that is an acceptable default; the detector can still be used in experiments.

4. TIME MEASUREMENT WITH A DSSSD

4.1 The microchannel plate detector (MCP)

Microchannel plate detectors [Ant99] were used as reference detectors for the time measurement of the W1(DS)-40 detector in the UNILAC accelerator experiment in cave X7.

A microchannel plate detector consists of an entrance window (a thin mylar foil), an electrostatic mirror and the position sensitive namesake microchannel plate, set up in a right triangle. Figure 4.1 shows a photo of one MCP; figure 4.2 a technical drawing.

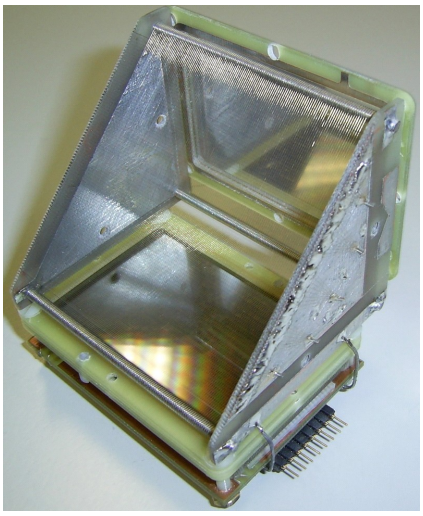

Fig. 4.1: Photo of one of the MCP detectors used in this experiment.

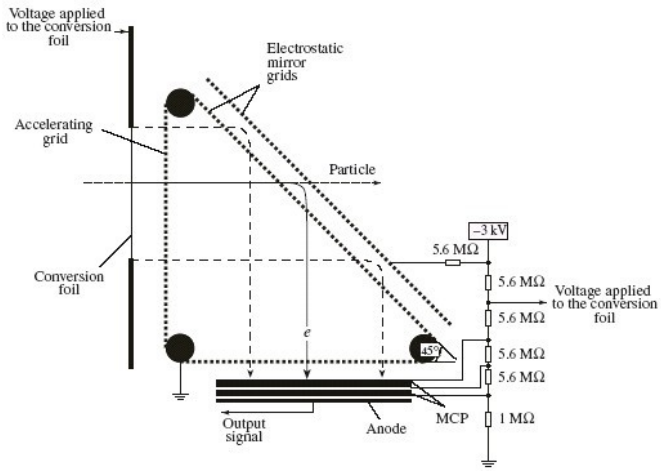

Fig. 4.2: Technical drawing of a MCP detector. [Kon08]

A heavy ion passing the foil will cause electrons to be emitted from it. The wire grid, which is inclined 45° away from the foil, creates an electric field, causing the electrons to fly towards the microchannel plate. The microchannel plate consists of a highly resistive material with tiny channels, about 10 μm in diameter and spaced apart by approximately 15 μm. An electron entering one of the channels, which are angled about 10° from the plate's orthogonal, will hit the wall of the channel multiple times, each time creating additional free electrons. A high voltage (2400 V and 2500 V) is applied to each MCP, to attract the electrons through the plate. At its other side, the cascade of electrons is detected by additional means, often simply a metal anode. MCP detectors produce pulses with varying lengths and heights, but with a very low time jitter, which makes them ideal for time measurements. They do however tend do produce a very large random noise and therefore require another particle detector as a trigger.

4.2 The setup for the UNILAC-experiment

A ^{48}Ca-beam at 5.9 MeV/u is impinged on a gold target of 0.09 μm. All detectors are mounted in a vacuum vessel at an angle of 20° relative to the beam direction to detect the scattered particles. The setup consisted of three detectors; two microchannel plate detectors and the aforementioned W1(DS)-40. Three signals are taken from the microchannel plate detectors; one each for time, x- and y-position. The time signal gets split up; one part is fed directly to a Philips 715 constant fraction differential discriminator (CFDD) and from there to a CAEN V1290A multihit-TDC (time-to-digital-converter) as a start/stop signal for the time-of-flight measurement. The Philips CFDD has a walk of ±75 ps; the CAEN TDC a time resolution of 25 ps. The other part of the time signal goes to a CAEN V792 QDC (charge-to-digital-converter) to determine the signal height and allow for a later walk correction. The two position signals pass a specially built fast preamplifier before also being fed into a CFDD and then into the TDC. One side of the DSSSD is connected as before, to a MPR-32 preamplifier, a STM-16 (energy branch) shaper and then to the CAEN V785AF ADC in order to measure the energy of the heavy ions. For the time branch, the other side of the DSSSD was used and two different electronics were connected. One includes a preamplifier and CFDD specially built by Wolfgang König from GSI. The output of the CFDD was then connected to the TDC. A second preamplifier was also tested, the so-called MFA-32, a fast preamplifier built by Mesytec.

As a start for the measurement, the trigger output from the STM-16 was used even if measurements only between the two MCPs were performed. This is necessary to suppress the large noise from the MCPs, which led to a high rate of random coincidences during test measurements. The complete block diagram of the time measurement is displayed in figure 4.3.

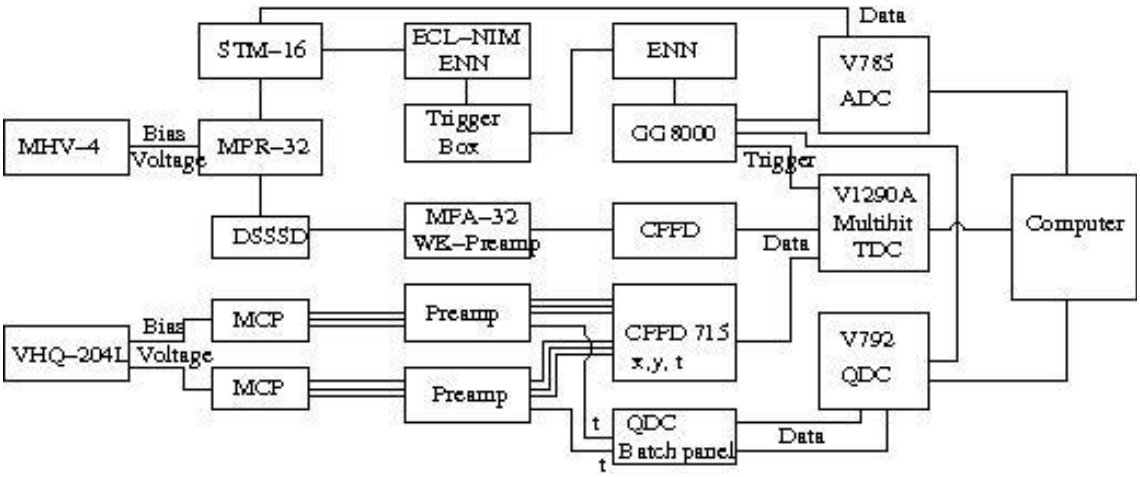

Fig. 4.3: The block diagram for the UNILAC experiment with an energy branch, consisting of a MPR-32 preamplifier, a STM-16 shaper and a V785 ADC, and a time branch, consisting of two different amplifiers and CFDDs and a V1290A multihit-TDC

4.3 Time measurement with two microchannel plate detectors

Two microchannel plate detectors were used for the time measurement. The time resolution σ_{tot} between two detectors is influenced by the resolution σ_i of each of the two detectors using the following formula:

$$\sigma_{tot} = \sqrt{\sigma_1^2 + \sigma_2^2} \tag{4.1}$$

It is assumed that the performance of the two MCPs is the same, which simplifies the formula to:

$$\sigma_{tot} = \sqrt{2\sigma^2} = \sqrt{2}\sigma \tag{4.2}$$

Solving for σ, which is the time resolution of a single MCP, we obtain:

$$\sigma = \frac{\sigma_{tot}}{\sqrt{2}} \tag{4.3}$$

In a first step, the time resolution between both MCPs was determined using all the data collected over the whole DSSSD, yielding:

$$\sigma = (144 \pm 11)ps \tag{4.4}$$

In a second step, the time resolution was determined for individual pixels of the DSSSD. There are two good reasons for doing this analysis: First, we discovered small, burn-like spots on the MCP before the experiment; probably from a prior use, which may or may not influence the time resolution. Second, the flight path of the ions is of course a different one for different positions on the detector. This slightly longer or shorter flight path is already sufficient to substantially change our time resolution.

Therefore, the time resolution was evaluated again by gating on single pixels of the silicon detector. This was done for 35 pixels, which were distributed evenly across the surface of the detector. A mean time resolution for the MCP yields:

$$\sigma = (75.8 \pm 4.0)ps \tag{4.5}$$

$$FWHM = (178.5 \pm 9.4)ps \tag{4.6}$$

Indeed, we find all used 35 pixels within this error limit. A typical time spectrum is displayed in figure 4.4 for strip 7 (time branch) and strip 8 (energy branch).

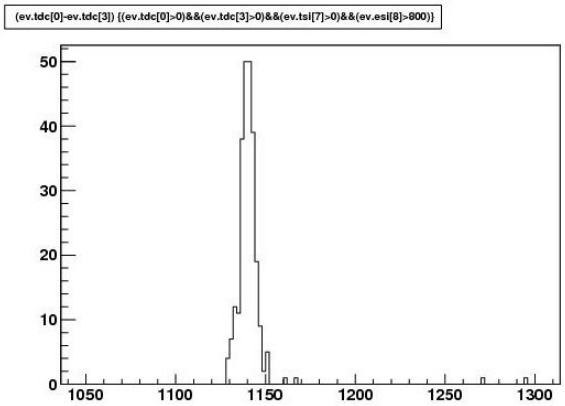

Fig. 4.4: Time spectrum between the two MCPs with a gate on pixel 7 (time branch):8 (energy branch) of the DSSSD

4.4 Time resolution between MCP and DSSSD using the new GSI preamplifier

After measuring a reference between two MCPs, the time resolution was now measured between one MCP and the DSSSD. A new preamplifier and a matching discriminator, both built by Wolfgang König of GSI (see [BLM15H], [S66], figure 4.5 and appendix C), were used to perform this measurement. The data were analysed in two steps: first, an estimation of the time resolution that can theoretically be reached with this setup; second, the time resolution actually obtained in this experiment.

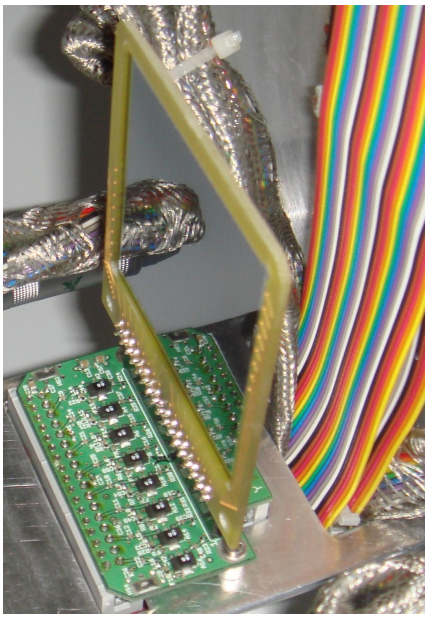

Fig. 4.5: The DSSSD mounted on the new preamplifier.

4.4.1 Estimating the best possible time resolution

Typical signals obtained from the preamplifier showed a rise time of 3 ns and a signal height of around 60 mV (see figures 4.6 and 4.7)

From the form of the signal, more accurately from the RMS (root mean square, also known as quadratic mean) noise and the slope of the pulse, a best possible time resolution can be estimated. The slope around the triggering point can be approximated as a linear function:

$$V(t) = a + bt \tag{4.7}$$

$$t = \frac{V - a}{b} \tag{4.8}$$

The variation of the triggering time is depending on the noise, therefore:

$$t_1 = \frac{(V - \Delta V) - a}{b} \tag{4.9}$$

$$t_2 = \frac{(V - \Delta V) + a}{b} \tag{4.10}$$

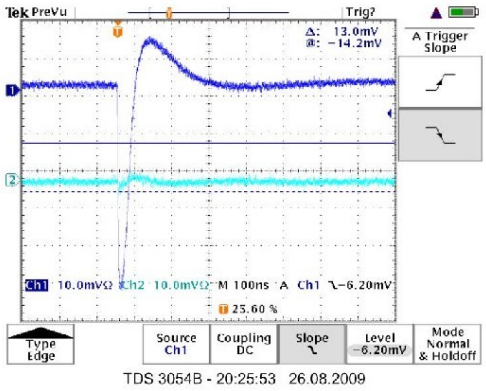

Fig. 4.6: A typical signal from strip 8 (dark blue) of the preamplifier. Note the well visible smaller signal in strip 7 (light blue); a cross-talk signal.

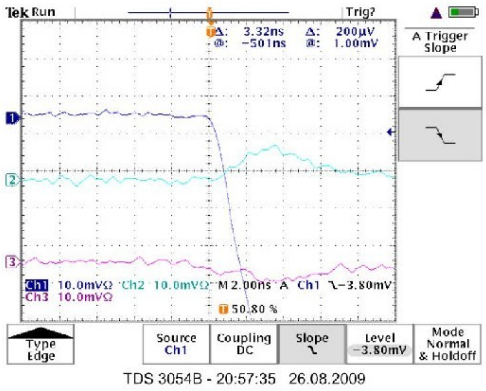

Fig. 4.7: Magnification of a signal from strip 2. Risetime can be estimated as 600 ps in an interval of 20 mV

The difference of the two gives Δt, which is:

$$\Delta t = \frac{2\Delta V}{b} \tag{4.11}$$

ΔV is the RMS noise, b is the slope of the front. The thresholds were set to -7.8 mV. The slope was determined via linear regression with Excel; the RMS is

$$\Delta V = V_{RMS} = \sqrt{\frac{1}{n}\sum_{i=1}^{n}(V_i - V_M)^2} \tag{4.12}$$

and was also calculated with Excel. V_M is the arithmetic mean of the baseline before the income of the signal. It has to be substracted from each value to compensate for the offset of the baseline.

The results for each strip are given in table 4.1.

From these data one obtains an estimate for the time resolution of:

$$\Delta t = 110.12ps \tag{4.13}$$

No data could be taken from six (1, 3, 9, 11, 13, 15) of the channels, due to faulty cable polarity. The signals coming from these channels were inverted on the oscilloscope, but data taking with the TDC was not influenced.

Strip two gave a rather bad resolution. Two pulses were usually documented for each strip. Unfortunately, only the magnified picture 4.7 was recorded, which did not allow detailed analysis. However, from figure 4.7, it is possible to estimate a slope of approximately 0.03 mV/ps. If the same noise as for the first signal is assumed, a time resolution of 30 ps can be calculated. We have not yet been able to explain the bad signal from strip two. Cross-talk between channels, especially neighbouring strips, has been observed, but typical cross-talk signals are about a factor of two smaller than the pulse from strip two.

The analysis does however show, that it seems to be possible to obtain a good time resolution with strip two.

Strip	Slope in mV/ps	Δ V in mV	Δ t in ps
0	0.0140	0.509	72.48
1	-	-	-
2	0.0021	0.499	470.10
3	-	-	-
4	0.0209	0.503	48.24
5	0.01	0.535	107.44
6	0.0063	0.587	186.45
7	0.0274	0.525	38.32
8	0.013	0.537	82.83
9	-	-	-
10	0.007	0.516	147.63
11	-	-	-
12	0.0029	0.729	183.05
13	-	-	-
14	0.0121	0.755	124.78
15	-	-	-

Tab. 4.1: shows the strip number, slope of the pulse ΔV and estimated time resolution

4.4.2 Results from the time measurement

A raw time spectrum of one strip shows a multiple peak structure (see figure 4.8). This result is due to the fact, that the created charge carriers need a certain time to migrate towards the electrodes. We have as yet no explanation for the non-linearity. Therefore, the data were again analysed pixel by pixel.

We have very little cross-talk in time and the cross-talk signals are so small that a condition on the energy signals is sufficient to exclude them. Only signals with an energy higher than channel 800 (910 and 930 for energy strips 0 and 1) were included. There is little to no data in energy strips 12-15. These were shielded from the source due to the experiment's geometry.

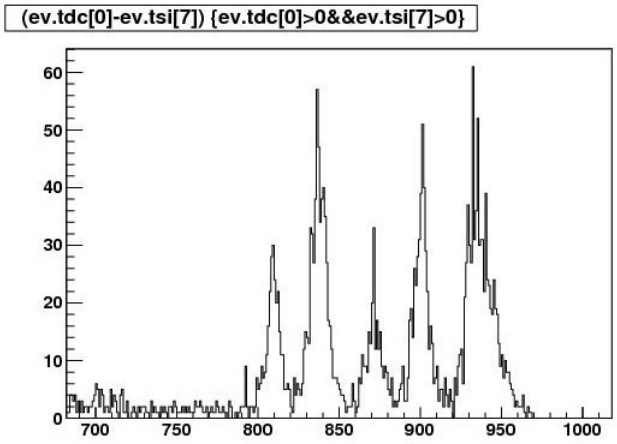

Fig. 4.8: The time-of-flight between MCP 1 and time strip 7 of the DSSSD without the gate on a pixel. The unit of the x-axis is channels; each channel corresponds to 25 ps. The five time peaks can be assigned to the energy strips 0 & 1, 2 & 3, 4 & 5, 6 & 7 and 8, 9, 10 & 11, respectively.

The time spectra for individual pixels of the DSSSD show only a single time peak, see figure 4.9.

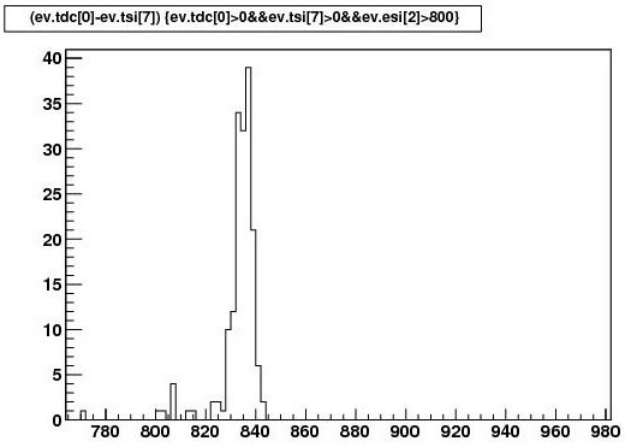

Fig. 4.9: The time of flight between MCP 1 and time strip 7, energy strip 2 of the DSSSD

Since two time of flights for each pixel are obtained, one for each of the two MCPs, a weighted mean for each pixel was calculated. First, by calculating the time resolution of the DSSSD without the MCP:

$$\sigma_{Si} = \sqrt{\sigma_{tot}^2 - \sigma_{MCP}^2} \tag{4.14}$$

An error is also given by ROOT's fit function; this was used to calculate an error for the resolution. The formula was obtained with standard error propagation (see also equation 4.4):

$$\delta\sigma_{Si} = \sqrt{(\frac{\partial\sigma}{\partial\sigma_{tot}}\delta\sigma_{tot})^2 + (\frac{\partial\sigma}{\partial\sigma_{MCP}}\delta\sigma_{MCP})^2} = \sqrt{\delta\sigma_{tot}^2 + \frac{1}{2}(\delta\sigma_{MCP})^2} \tag{4.15}$$

The weighted mean is given as:

$$\bar{\sigma} = \frac{\sigma_1(\frac{1}{\delta\sigma_1^2}) + \sigma_2(\frac{1}{\delta\sigma_2^2})}{(\frac{1}{\delta\sigma_1^2}) + (\frac{1}{\delta\sigma_2^2})} \tag{4.16}$$

Time resolutions vary between 26 ps and 186 ps. This is also the range for time resolutions that the preliminary estimation yielded (see table 4.1; here it is 30 to 183 to be precise). Calculating then a mean of all pixels, we obtain:

$$\sigma = (54 \pm 34)ps \tag{4.17}$$

$$FWHM = (127 \pm 80)ps \tag{4.18}$$

This even includes two strips (energy 5 and time 8) in which much less data was collected. Therefore, the time resolution is strongly degraded. It is, however, much better than the estimation. The already familiar problem of edge strips was again observed. Exemplary results for one time strip (strip 7) can be found in appendix B.

4.5 Testing the Mesytec MFA-32

The MFA-32 is a 32 channel fast amplifier prototype from the company Mesytec [Mes]. It has eight fast outputs, each of them the sum of four neighbouring channels; the exact position is internally coded. The input has to be positive; the output is negative so as to allow further processing with a constant fraction discriminator. The preamplifier is optimised for high energy depositions, typically 100 MeV to 2 GeV. The datasheet can be found in appendix C.

The MFA-32 was first tested with electrons from a ^{207}Bi-source. One output from the chamber was connected to the MPR-32; the other one to the MFA-32. Since the MFA-32 does not have an input for detector bias voltage, the detector had to be biased via the MPR-32. The two preamplifiers must have a ground connection and the side of the detector on which the bias voltage is put must be the one connected to the MPR-32. Since the MFA-32 needs positive input signals, a negative bias voltage must be applied, so that the negative signals can be given to the MPR-32. However, the conversion electrons deposit too little energy in the detector and little or no signals can be seen in the output of MFA-32.

The test was therefore repeated in the steal chamber using α-particles from a ^{241}Am-source. Now, small peaks can be observed, as seen in figure 4.10. The α-particles emitted by ^{241}Am have an energy of approximately 5.4 MeV, which is still far below the required 100 MeV, and the observed peaks are hardly higher than the noise and far too small to be processed.

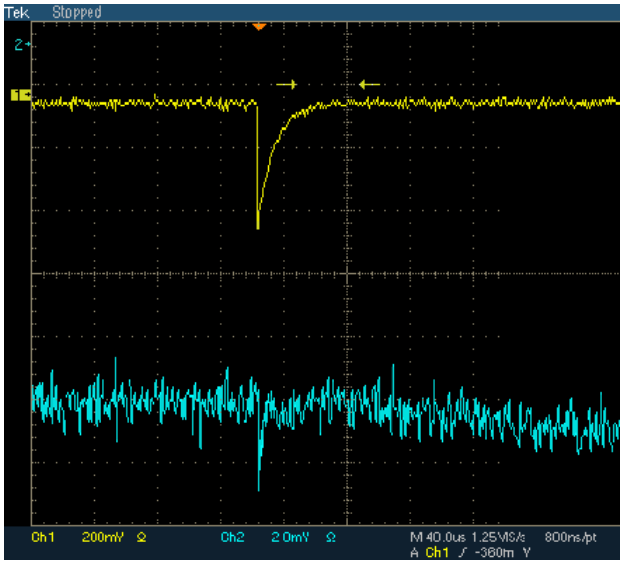

Fig. 4.10: The signal from the MPR-32 (1, yellow) and the MFA-32 (2, blue) obtained with a ^{241}Am-source

The preamplifier was therefore tested with a ^{48}Ca-beam at 5.9 MeV/u. A typical puls obtained can be seen in picture 4.11. Channel one shows the signal from the MPR-32, channel two the signal from the MFA. The signals still do not reach 10 mV and a risetime of about 100 ns can be determined from picture 4.12. The energy deposition still does not seem large enough to obtain signals that can be processed. With a revised version of MFA-32 we hope to obtain a pulse with a higher magnification.

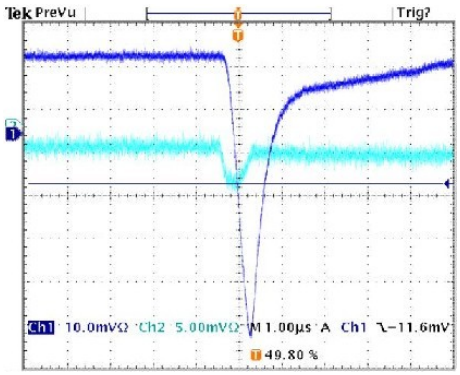

Fig. 4.11: Energy signal in channel 1 (dark blue), time signal in channel 2 (light blue)

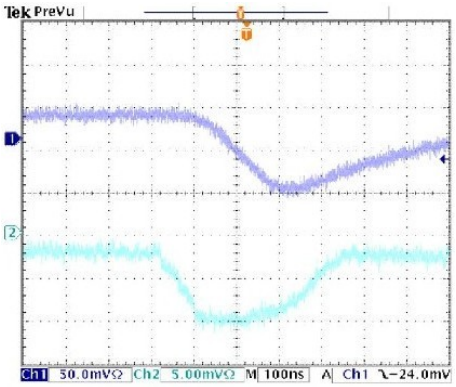

Fig. 4.12: Energy signal in channel 1 (dark blue), time signal in channel 2 (light blue). The risetime of the timing signal is approximately 100 ns.

5. SUMMARY AND OUTLOOK

DSSSDs yield usually a position resolution which is better than the strip width - in our case 3 mm. A heavy ion usually deposits its energy over more than one strip and from the centroid of the distribution the position is determined. The obtained energy resolution was typical 1.8 % for a 1 MeV conversion electron line and 0.6 % for a 5 MeV α-line. In an accelerator experiment with Ca-ions at an energy of 5.9 MeV/u a time resolution of 54 ps was obtained. The large variation for the different strips is not yet explained. The promising results obtained at rather low energies suggests new test measurements at 100 MeV/u at which all scattering experiments of the PRESPEC-campaign will be performed.

The outcome of the future test will most likely reduce the number of detectors close to the target to one DSSSD for position, energy and time measurement.

APPENDIX

A. DETAILED RESULTS FOR THE ACTIVE STOPPER DETECTORS 2524-21, 2536-3, 2524-24, 2540-21, 2512-17, 2243-3

Strip	Peak 1	Peak 2	FWHM	dE/keV	dE/%	Slope	Offset
X1	1203,65	2407,24	46,1227	18,9305	1,9160	0,4104	-12,325
X2	1148,85	2322,98	41,5969	17,5014	1,7909	0,4207	-1,6638
X3	1259,75	2515,53	41,2928	16,2438	1,6415	0,3934	-13,862
X4	1247,18	2514,78	41,8103	16,2941	1,6626	0,3897	-4,3421
X5	1177,88	2338,44	37,1994	15,8342	1,5908	0,4257	-19,672
X6	1230,62	2448,73	38,9411	15,7924	1,5903	0,4055	-17,373
X7	1180,16	2397,24	41,3947	16,8017	1,7268	0,4059	2,6854
X8	1169,44	2355,88	39,2130	16,3272	1,6645	0,4164	-5,2217
X9	1228,55	2469,68	39,2206	15,6108	1,5881	0,3980	-7,2929
X10	1193,69	2388,63	38,0067	15,7124	1,5912	0,4134	-11,783
X11	1208,23	2430,33	42,3785	17,1303	1,7437	0,4042	-6,6934
X12	1176,04	2367,12	38,8504	16,1132	1,6413	0,4148	-6,0622
X13	1258,69	2489,42	42,6143	17,1049	1,7118	0,4014	-23,523
X14	1273,63	2537,61	40,5998	15,8676	1,5999	0,3908	-16,072
X15	1258,65	2512,48	42,2737	16,6555	1,6825	0,3940	-14,199
X16	1210,11	2439,10	39,9216	16,0467	1,6367	0,4019	-4,7111
Y1	1246,06	2452,32	52,1469	21,3557	2,1264	0,4095	-28,599
Y2	1147,47	2271,65	44,4695	19,5413	1,9576	0,4394	-22,534
Y3	1245,76	2465,12	49,9840	20,2501	2,0277	0,4051	-22,996
Y4	1157,17	2305,79	45,3707	19,5131	1,9677	0,4301	-15,977
Y5	1044,29	2178,45	45,0656	19,6289	2,0687	0,4356	26,844
Y6	1250,89	2479,70	54,0482	21,7282	2,1796	0,4020	-21,177
Y7	1203,68	2363,58	46,7109	19,8941	1,9762	0,4259	-30,946
Y8	1203,56	2389,61	50,2279	20,9204	2,1019	0,4165	-19,593
Y9	1152,08	2273,52	46,8795	20,6507	2,0620	0,4405	-25,797
Y10	1146,68	2282,39	41,8363	18,1976	1,8331	0,4349	-17,072
Y11	1207,38	2372,46	42,9884	18,2273	1,8120	0,4240	-30,235
Y12	1219,27	2399,69	47,9422	20,0636	1,9979	0,4185	-28,559
Y13	1209,22	2389,16	46,0149	19,2649	1,9260	0,4187	-24,559
Y14	1208,18	2405,67	46,3900	19,1373	1,9284	0,4125	-16,710
Y15	1259,28	2463,92	46,9169	19,2397	1,9042	0,4101	-34,707
Y16	1230,23	2379,31	47,6193	20,4720	2,0014	0,4299	-47,187

Tab. A.1: Detailed results for detector 2524-21

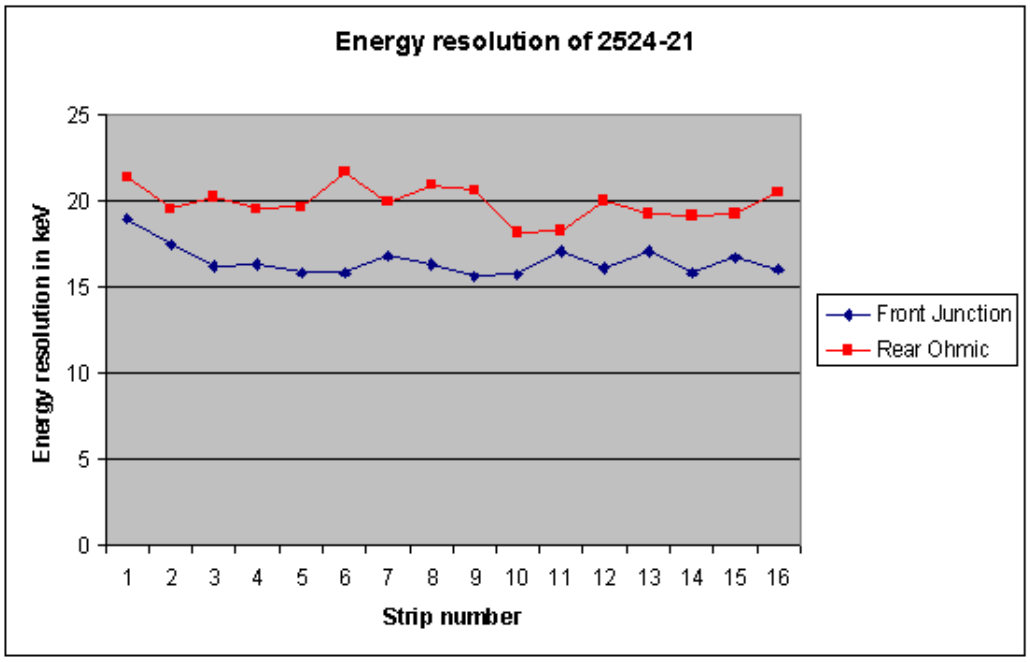

Fig. A.1: Energy resolution versus strip number for detector 2524-21

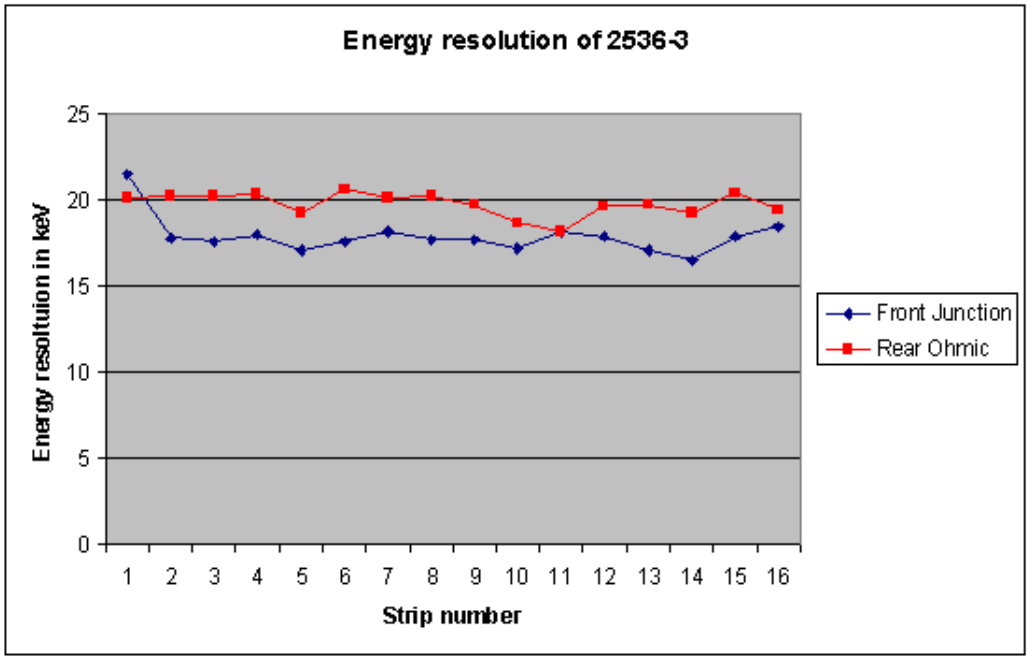

Fig. A.2: Energy resolution versus strip number for detector 2536-3

Strip	Peak 1	Peak 2	FWHM	dE/keV	dE/%	E/CH	Offset
X1	1212,21	2406,60	51,9071	21,4688	2,1569	0,4136	-19,670
X2	1153,57	2319,26	41,8338	17,7285	1,8038	0,4238	-7,1637
X3	1262,62	2514,64	44,5100	17,5619	1,7700	0,3946	-16,482
X4	1250,01	2513,01	45,8829	17,9463	1,8258	0,3911	-7,2192
X5	1181,44	2337,78	40,0822	17,1235	1,7145	0,4272	-23,023
X6	1232,07	2447,48	43,2429	17,5759	1,7668	0,4064	-19,071
X7	1181,62	2396,47	44,6484	18,1556	1,8631	0,4067	1,2125
X8	1173,21	2355,06	42,3118	17,6859	1,7966	0,4179	-8,6886
X9	1230,36	2468,09	44,2654	17,6671	1,7935	0,3991	-9,3585
X10	1196,61	2387,12	41,3671	17,1652	1,7329	0,4149	-14,831
X11	1214,24	2429,38	44,6807	18,1644	1,8392	0,4065	-11,934
X12	1181,59	2365,40	42,8272	17,8717	1,8106	0,4173	-11,374
X13	1260,66	2489,50	42,3853	17,0454	1,7029	0,4022	-25,277
X14	1279,39	2536,88	42,0442	16,5169	1,6573	0,3928	-20,903
X15	1264,17	2510,92	45,2001	17,9096	1,8001	0,3962	-19,202
X16	1209,90	2436,20	45,7140	18,4153	1,8764	0,4028	-5,6935
Y1	1243,05	2451,93	49,2448	20,1235	2,0084	0,4086	-26,263
Y2	1145,37	2271,31	46,1461	20,2464	2,0317	0,4387	-20,825
Y3	1245,85	2464,83	49,8797	20,2141	2,0237	0,4053	-23,189
Y4	1155,52	2305,26	47,2030	20,2814	2,0476	0,4297	-14,783
Y5	1042,02	2178,64	44,3155	19,2605	2,0341	0,4346	28,815
Y6	1250,11	2481,05	51,3005	20,8579	2,0677	0,4013	-19,993
Y7	1204,90	2364,74	47,2138	20,1093	1,9966	0,4259	-31,492
Y8	1204,81	2391,41	48,5377	20,2070	2,0297	0,4163	-19,881
Y9	1151,18	2275,19	44,8961	19,7317	1,9733	0,4395	-24,241
Y10	1147,65	2282,80	42,9059	18,6720	1,8795	0,4352	-17,740
Y11	1206,29	2372,59	42,8355	18,1435	1,8054	0,4236	29,238
Y12	1218,75	2400,13	46,9412	19,6287	1,9558	0,4182	-27,926
Y13	1209,33	2389,70	47,0343	19,6845	1,9682	0,4185	-24,420
Y14	1208,20	2405,77	46,6845	19,2575	1,9405	0,4125	-16,685
Y15	1257,70	2462,46	49,8077	20,4232	2,0227	0,4101	-34,008
Y16	1202,30	2379,17	46,2718	19,4229	1,9449	0,4198	-22,974

Tab. A.2: Detailed results for detector 2536-3

Strip	Peak 1	Peak 2	FWHM	dE/keV	dE/%	E/CH	Offset
X1	1215,26	2410,20	51,1091	21,1291	2,1205	0,4134	-20,701
X2	1158,66	2322,66	46,2502	19,2041	1,9482	0,4244	-10,034
X3	1268,89	2518,47	44,8386	17,7262	1,7804	0,3953	-19,934
X4	1255,34	2516,84	47,3867	18,5565	1,8828	0,3916	-9,8878
X5	1185,91	2341,71	42,0564	17,9753	1,7960	0,4274	-25,169
X6	1237,58	2451,66	44,4201	18,0742	1,8118	0,4069	-21,862
X7	1188,00	2401,33	47,1885	19,2125	1,9651	0,4071	-1,9870
X8	1177,54	2358,54	44,9454	18,8002	1,9056	0,4183	-10,853
X9	1237,10	2472,22	45,6558	18,2606	1,8468	0,3999	-13,092
X10	1203,21	2391,20	44,3843	18,4563	1,8562	0,4158	-18,629
X11	1223,13	2433,46	47,8653	19,5364	1,9670	0,4082	-17,524
X12	1186,05	2369,98	44,3311	18,4974	1,8705	0,4173	-13,185
X13	1264,69	2492,30	45,7434	18,4075	1,8354	0,4024	-27,221
X14	1284,14	2540,09	48,4616	19,0613	1,9079	0,3933	-23,388
X15	1267,86	2513,84	48,2808	19,1421	1,9206	0,3965	-20,975
X16	1214,15	2436,99	54,5706	22,0453	2,2393	0,4040	-8,7894
Y1	1247,19	2453,19	55,0053	22,5312	2,2422	0,4096	-29,172
Y2	1148,09	2273,39	49,4378	21,7029	2,1746	0,4390	-22,305
Y3	1248,19	2466,60	54,4233	22,0657	2,2064	0,4054	-24,374
Y4	1157,75	2306,87	46,3363	19,9197	2,0086	0,4299	-16,010
Y5	1045,64	2178,99	47,1519	20,5524	2,1639	0,4359	25,931
Y6	1251,71	2481,26	53,7543	21,5970	2,1664	0,4018	-21,203
Y7	1204,51	2364,46	47,6682	20,3010	2,0161	0,4259	-31,277
Y8	1205,03	2389,36	51,8074	21,6096	2,1683	0,4171	-20,934
Y9	1154,82	2277,23	48,1248	21,1809	2,1133	0,4401	-26,564
Y10	1150,23	2284,80	46,0139	20,0348	2,0139	0,4354	-19,118
Y11	1211,92	2374,33	46,6082	19,8075	1,9630	0,4249	-33,341
Y12	1223,70	2402,52	49,8296	20,8818	2,0741	0,4191	-31,108
Y13	1213,20	2392,39	49,5829	20,7719	2,0725	0,4189	-26,548
Y14	1211,31	2408,05	49,5570	20,4566	2,0580	0,4128	-18,314
Y15	1261,54	2465,24	50,5317	20,7383	2,0498	0,4104	-36,068
Y16	1206,94	2381,35	48,7667	20,5131	2,0479	0,4206	-25,983

Tab. A.3: Detailed results for detector 2524-24

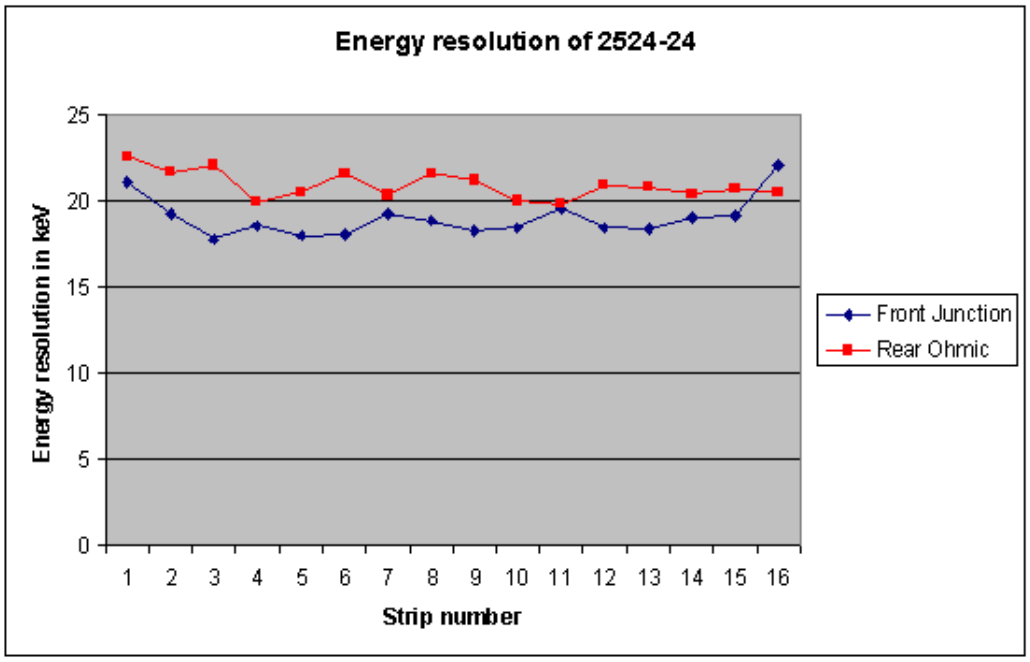

Fig. A.3: Energy resolution versus strip number for detector 2524-24

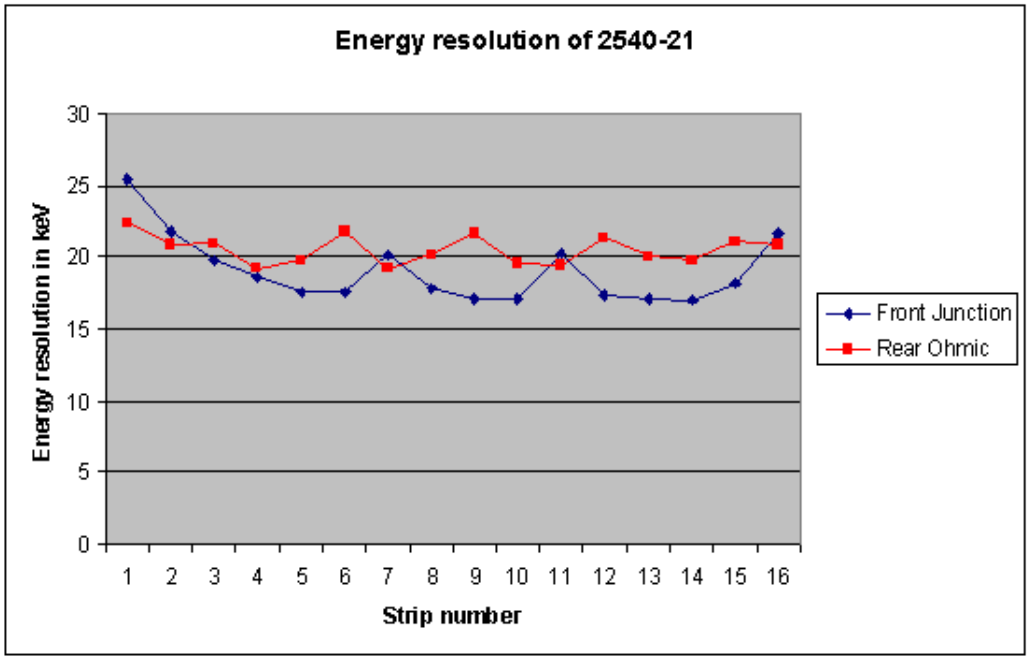

Fig. A.4: Energy resolution versus strip number for detector 2540-21

Strip	Peak 1	Peak 2	FWHM	dE/keV	dE/%	E/CH	Offset
X1	1206,42	2402,93	61,5583	25,4154	2,5618	0,4129	-16,392
X2	1150,26	2316,61	51,4277	21,7819	2,2199	0,4235	-5,4852
X3	1260,55	2512,85	50,0689	19,7667	1,9925	0,3948	-16,237
X4	1248,15	2512,53	47,8079	18,6788	1,9028	0,3907	-5,9589
X5	1180,66	2337,39	41,1188	17,5604	1,7592	0,4271	-22,520
X6	1232,46	2448,49	43,1973	17,5484	1,7642	0,4062	-18,975
X7	1152,87	2397,88	49,4704	20,1137	2,0631	0,4066	0,7675
X8	1173,13	2356,67	42,5589	17,7637	1,8059	0,4174	-7,9549
X9	1232,14	2470,21	42,7356	17,0519	1,7301	0,3990	-9,9339
X10	1199,22	2390,03	41,3773	17,1651	1,7312	0,4148	-15,789
X11	1216,26	2431,77	49,7464	20,2176	2,0457	0,4064	-12,605
X12	1183,98	2369,11	41,6562	17,3636	1,7583	0,4168	-11,821
X13	1263,66	2492,22	42,4123	17,0539	1,7018	0,4021	-26,414
X14	1284,36	2541,52	43,3804	17,0463	1,7069	0,3929	-22,988
X15	1268,05	2515,79	45,8875	18,1676	1,8240	0,3959	-20,341
X16	1215,35	2469,33	53,8522	21,7348	2,2077	0,4036	-8,8169
Y1	1239,59	2442,54	54,4099	22,3438	2,2276	0,4107	-27,346
Y2	1143,10	2264,41	47,4311	20,8961	2,0946	0,4406	-21,900
Y3	1242,93	2456,76	51,5211	20,9679	2,0971	0,4070	-24,143
Y4	1155,71	2300,34	44,5543	19,2288	1,9369	0,4316	-17,082
Y5	1043,00	2163,58	45,2512	19,7897	2,0915	0,4373	29,500
Y6	1250,99	2474,94	53,8647	21,7404	2,1764	0,4036	-23,214
Y7	1205,95	2360,99	44,9755	19,2356	1,9049	0,4277	-34,074
Y8	1207,71	2387,54	48,1067	20,1425	2,0149	0,4187	-23,973
Y9	1142,10	2262,88	49,2944	21,7272	2,1784	0,4408	-21,697
Y10	1139,29	2271,52	44,7317	19,5168	1,9692	0,4363	-15,380
Y11	1200,75	2361,74	45,5824	19,3953	1,9300	0,4255	-29,218
Y12	1212,39	2388,56	50,8052	21,3356	2,1270	0,4200	-27,513
Y13	1203,36	2379,69	47,7272	20,0431	2,0056	0,4100	-23,651
Y14	1202,89	2396,22	47,8614	19,8131	1,9973	0,4140	-16,258
Y15	1253,03	2452,78	51,1785	21,0729	2,0866	0,4118	-34,238
Y16	1198,62	2370,28	49,4217	20,8374	2,0851	0,4216	-23,667

Tab. A.4: Detailed results for detector 2540-21

Strip	Peak 1	Peak 2	FWHM	dE/keV	dE/%	E/CH	Offset
X1	1219,92	2412,55	62,5849	25,9233	2,5941	0,4142	-23,604
X2	1161,94	2327,17	50,5886	21,4471	2,1738	0,4240	-10,905
X3	1275,47	2526,24	44,5065	17,5781	1,7618	0,3950	-22,055
X4	1262,44	2523,92	47,0104	18,4094	1,8626	0,3916	-12,676
X5	1192,66	2347,12	39,8997	17,0733	1,6999	0,4279	-28,646
X6	1245,47	2457,93	43,4372	17,6979	1,7672	0,4074	-25,749
X7	1194,96	2406,83	49,1484	20,0346	2,0420	0,4076	-5,4069
X8	1185,24	2364,52	43,3438	18,1567	1,8331	0,4189	-14,797
X9	1242,54	2480,17	40,4113	16,1302	1,6294	0,3992	-14,260
X10	1209,10	2397,13	40,6566	16,9056	1,6961	0,4158	-21,061
X11	1219,78	2433,24	53,3751	21,7290	2,1936	0,4071	-14,873
X12	1192,40	2374,21	54,3180	22,7051	2,2878	0,4180	-16,727
X13	1270,51	2496,11	42,7065	17,2136	1,7109	0,4031	-30,402
X14	1269,01	2524,35	67,8438	26,6978	2,6876	0,3935	-17,679
X15	1273,85	2520,10	48,8657	19,3698	1,9390	0,3964	-23,240
X16	1219,62	2441,52	64,1514	25,9357	2,6275	0,4043	-11,378
Y1	1237,14	2428,39	68,2803	28,3152	2,8118	0,4147	-31,330
Y2	1142,69	2254,93	49,5752	22,0188	2,1985	0,4441	-25,824
Y3	1241,12	2446,50	54,9579	22,5234	2,2464	0,4098	-26,947
Y4	1152,59	2290,69	45,9037	19,9248	2,0039	0,4341	-18,589
Y5	1034,18	2158,01	48,0652	21,1279	2,2273	0,4396	27,107
Y6	1225,96	2445,29	60,3304	24,4423	2,4672	0,4051	-14,986
Y7	1199,47	2348,59	46,8764	20,1519	1,9959	0,4299	-33,945
Y8	1195,41	2372,01	60,5116	25,4060	2,5511	0,4199	-20,197
Y9	1147,12	2256,60	65,9046	29,3443	2,9205	0,4453	-29,059
Y10	1146,74	2270,76	44,4846	19,5507	1,9590	0,4395	-22,285
Y11	1207,80	2360,74	44,7226	19,1623	1,8944	0,4285	-35,806
Y12	1218,41	2384,81	51,8211	21,9476	2,1730	0,4235	-34,328
Y13	1206,76	2375,05	50,9550	21,5458	2,1454	0,4228	-28,567
Y14	1203,33	2384,59	64,1881	26,8433	2,6918	0,4182	-21,530
Y15	1245,29	2428,36	83,8110	34,9959	3,4513	0,4176	-38,280
Y16	1190,33	2347,08	74,9430	32,0051	3,1930	0,4271	-26,641

Tab. A.5: Detailed results for detector 2512-17

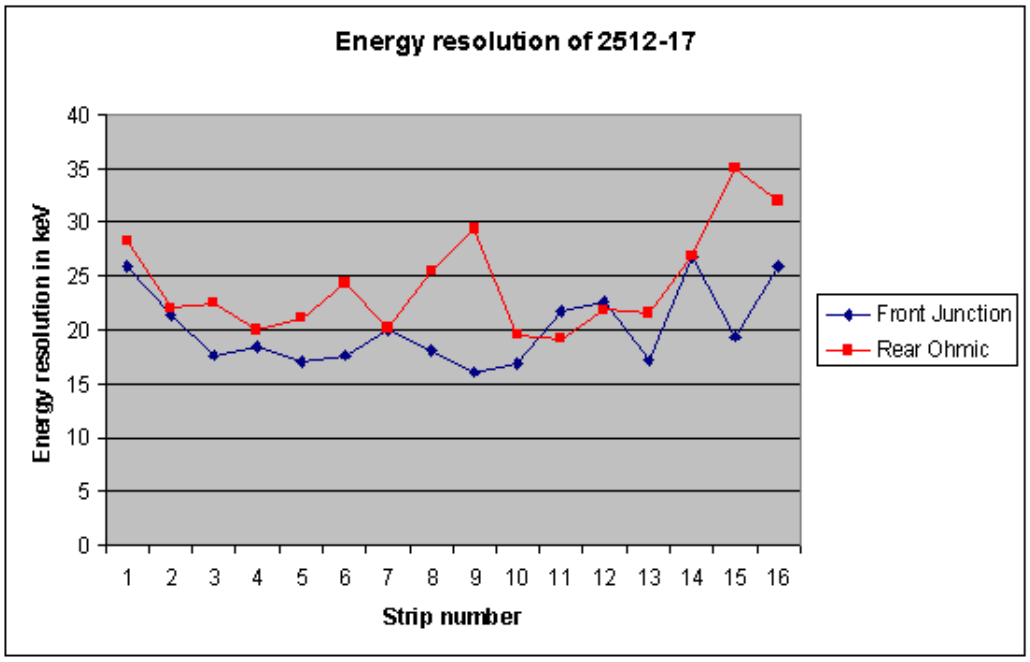

Fig. A.5: Energy resolution versus strip number for detector 2512-17

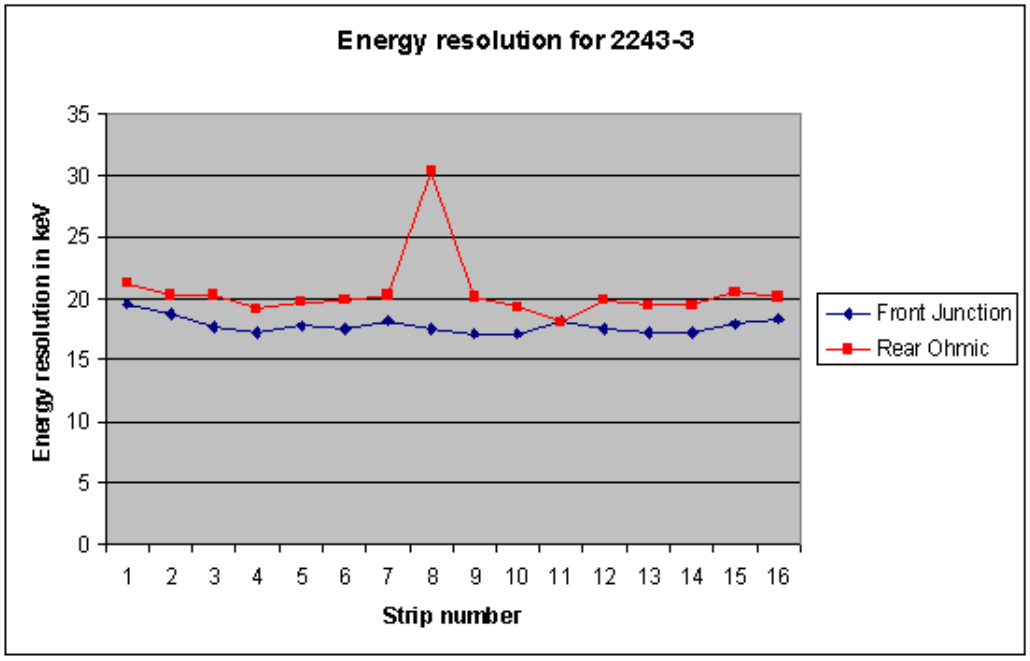

Fig. A.6: Energy resolution versus strip number for detector 2243-3

Strip	Peak 1	Peak 2	FWHM	dE/keV	dE/%	E/Ch	Offset
X1	1205,99	2405,36	47,6195	19,3162	1,9797	0,4119	-15,027
X2	1149,81	2316,06	44,1215	18,5873	1,9050	0,4236	-5,3363
X3	1261,56	2511,79	44,6388	17,3399	1,7772	0,3951	-16,777
X4	1247,58	2511,31	44,2001	17,1727	1,7601	0,3909	-5,9869
X5	1178,98	2335,14	41,5485	17,3604	1,7793	0,4273	-22,050
X6	1230,19	2445,12	43,0047	17,1606	1,7588	0,4066	-18,505
X7	1179,16	2393,93	44,7624	18,2439	1,8698	0,4066	2,1812
X8	1170,59	2353,30	41,8451	17,3494	1,7781	0,4177	-7,2377
X9	1227,81	2465,84	42,8332	16,9485	1,7370	0,3990	-8,2220
X10	1195,56	2385,00	41,3113	16,9004	1,7321	0,4153	-14,842
X11	1212,71	2426,98	44,6812	17,9628	1,8410	0,4068	-11,665
X12	1179,54	2363,97	41,8540	17,2747	1,7705	0,4171	-10,260
X13	1259,61	2486,46	42,7610	16,7796	1,7198	0,4027	-25,491
X14	1278,76	2535,06	43,7422	16,8356	1,7255	0,3932	-21,132
X15	1261,93	2509,92	45,0964	17,5307	1,7967	0,3958	-17,818
X16	1209,54	2435,72	45,5897	18,2623	1,8717	0,4029	-5,5961
Y1	1241,85	2449,84	51,7108	20,5949	2,1108	0,4089	-26,147
Y2	1143,42	2269,80	46,2473	19,8799	2,0375	0,4386	-19,773
Y3	1244,56	2461,84	49,9437	19,7942	2,0287	0,4058	-23,371
Y4	1154,87	2303,84	44,5677	18,8749	1,9345	0,4299	-14,837
Y5	1040,76	2175,68	45,1685	20,2562	2,0761	0,4352	28,936
Y6	1248.05	2478,50	49,2649	19,3939	1,9877	0,4015	-19,366
Y7	1202,33	2361,48	47,4986	19,6251	2,0114	0,4262	-30,702
Y8	1178,23	2350,27	71,9333	29,8627	3,0606	0,4215	-14,909
Y9	1149,68	2272,85	45,6908	19,6144	2,0103	0,4398	-23,959
Y10	1145,86	2279,53	44,1074	18,8792	1,9349	0,4358	-17,612
Y11	1206,33	2370,75	42,5501	17,5118	1,7948	0,4242	-30,080
Y12	1216,38	2377,95	47,1404	19,2882	1,9759	0,4181	-26,854
Y13	1208,07	2387,38	46,5030	19,0053	1,9479	0,4189	-24,347
Y14	1205,22	2403,09	47,2259	19,1746	1,9652	0,4124	-15,331
Y15	1256,37	2460,1	50,0661	19,8567	2,0351	0,4104	-33,903
Y16	1200,14	2377,07	47,9536	19,6832	2,0173	0,4197	-22,042

Tab. A.6: Detailed results for detector 2243-3

B. EXEMPLARY RESULTS FOR TIME STRIP 7

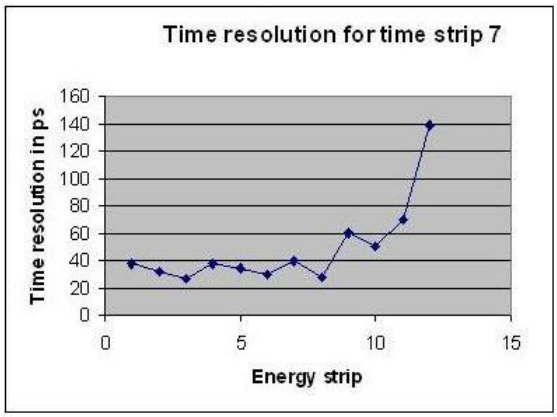

Fig. B.1: Time resolution versus energy strip number in time strip 7

Strip	σ_{M1-Si}	$\Delta\sigma_{M1-Si}$	σ_{M2-Si}	$\Delta\sigma_{M2-Si}$	σ_{Si1}	$\Delta\sigma_{Si1}$	σ_{Si2}	$\Delta\sigma_{Si2}$	σ_{Mean}
1	100.8	7.3	76.3	7.8	66.2	8.1	7.9	8.3	38.0
2	100.3	28.5	78.8	16.5	65.7	28.7	21.3	16.7	35.5
3	80.3	5.3	78.8	0.8	26.0	6.0	27.6	7.6	26.6
4	84.8	4.8	80.8	7.0	37.7	5.5	39.2	5.9	38.3
5	94.5	9.0	85.4	5.2	56.3	9.4	16.8	5.91	34.6
6	86.5	13.7	78.0	8.1	41.8	13.9	18.2	14.4	30.5
7	87.3	7.0	84.4	6.2	43.3	7.6	37.0	6.8	39.8
8	81.3	5.0	80.5	5.9	29.4	5.7	27.1	6.6	28.4
9	110.5	9.2	90.7	6.2	80.3	9.6	49.8	6.9	60.1
10	87.0	5.6	98.1	7.0	42.6	6.3	62.3	7.6	50.6
11	105.8	6.6	99.8	7.5	73.8	7.2	64.9	8	69.9
12	173.1	6.7	140.1	17.7	155.6	15.7	117.9	17.9	139.2

Tab. B.1: Detailed results for time strip 7 (all numbers in ps). The first four columns are the fit parameters from the spectra; the next four the two calculated time resolutions with their errors; the last column shows the weighted mean for each strip.

C. TECHNICAL DETAILS OF THE PREAMPLIFIERS

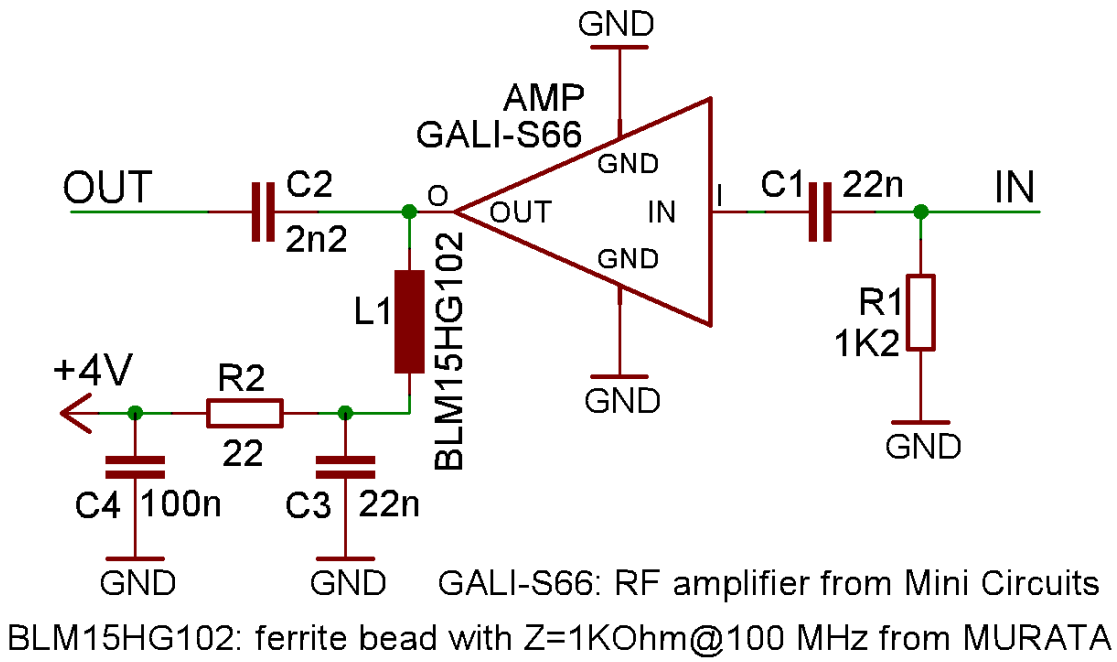

Fig. C.1: The detailed layout of one strip of the GSI preamplifier, provided by Wolfang König

mesytec

MFA-32

Datasheet V1.0

32 channel fast summing amplifier with position outputs

MFA-32 is a 32 channel high density fast amplifier optimised for silicon strip detectors with high energy deposition (typ. 100 MeV to 2 GeV). Its 8 fast ouputs provide an amlitude sum of 4 neighbouring channels each.
The position (channel hit by a particle) is coded as amplitude ratio of two tail pulse outputs. Position coding is internally implemented by converting the signals of 32 input amplifiers to a current, applying a soft threshold for noise reduction, and adding it to a resistor chain. Both ends of the resistor chain are amplified by a charge sensitive amplifier.

Inputs:

- 50 Ω terminated,
- AC-coupled (100 kΩ bias resistors to ground),
- Max. +350 mV (for MFA-32P type)

Fast outputs:
Typical signal processing: outputs connected to CFD, then to TDC

- 50 Ω outputs
- Sum of 4 input channels
- max. –2 V terminated
- Risetime 1.5 ns at 1 V output
- Gain = 5 (referenced to 1 input channel with particle hit)

Position outputs:
Typical signal processing: signals connected to shapers with 1us FWHM, then to peak sensing ADCs.

- 2 position outputs (pos0, pos31), representing the two ends of the resistor chain
- can be terminated with 50 Ω
- polarity: inverting
- risetime typ 30 ns, decay time 10 us
- position calculation: position = (pos0-pos1)/(pos0+pos1) + offset

Power supply:

- +6 V, 0.3 A
- -6 V, -0.3 A
- Total power = 4 W
- Connector SubD9, (standard mesytec)
  - pin 1, 2 = gnd,
  - pin 3 = +6 V,
  - pin 5 = -6 V

mesytec GmbH & co. KG
Wernher-von-Braun- Str. 1, D-85640 Putzbrunn, Germany
fon: +49 - 89 / 456007-30 fax: +49 - 89 / 456007-39
info@mesytec.com - www.mesytec.com

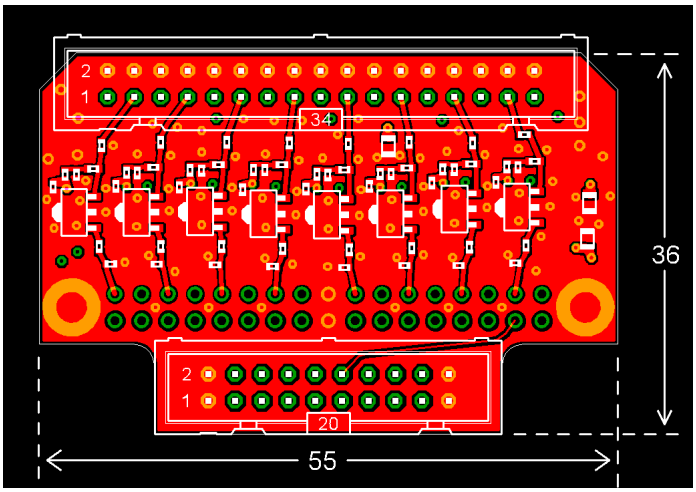

Fig. C.2: The layout of the top side of the GSI preamplifier, provided by Wolfang König

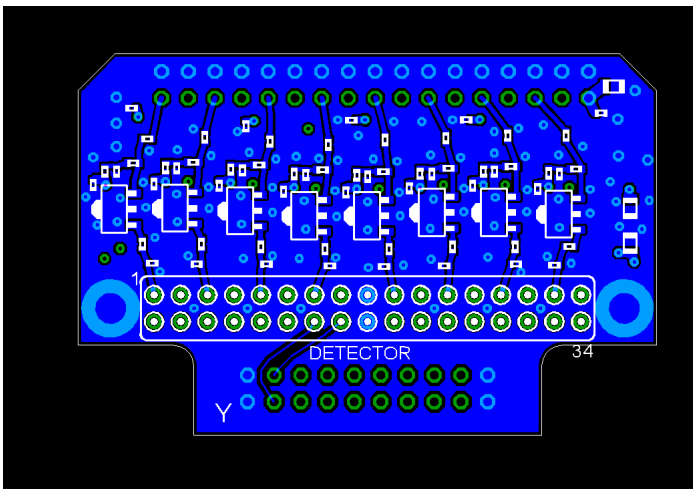

Fig. C.3: The layout of the bottom side of the GSI preamplifier, provided by Wolfang König

BIBLIOGRAPHY

[Gei92] H. Geissel et al., Nucl. Instrum. and Meth. B70 (1992)

[Sim97] J. Simpson, Z. Phys. A358 (1997), 139

[Pie07] S. Pietri et al., Nucl. Instrum. and Meth. B261 (2007), 1079

[Wol05] H. J. Wollersheim et. al., Nucl. Instrum. and Meth. A537 (2005), 637

[Pod08] Zs. Podolyák et. al., Nucl. Instrum. and Meth. B266 (2008), 4589-4594

[Kum09] R. Kumar et al., Nucl. Instrum. and Meth. A598 (2009), 754

[Rud08] D. Rudolph et al., Technical Report, V1.2, June 2008

[Kno00] Knoll, Glenn F.: Radiation Detection and Measurement; John Wiley & Sons, Inc., Third edition, 2000

[Kra05] M. Krammer, Vorlesung über "'Detektoren in der Hochenergiephysik"', ÖAW, Wien

[Micron] Micron Semiconductor Ltd. http://www.micronsemiconductor.co.uk/pdf/w1.pdf

[Mes] http://www.mesytec.com

[MPR32] http://www.mesytec.com/datasheets/MPR16.pdf

[STM16] http://www.mesytec.com/datasheets/STM-16.pdf

[MHV4] http://www.mesytec.com/datasheets/MHV-4.pdf

[MRC1] http://www.mesytec.com/datasheets/MRC-1.pdf

[ADC] http://www.caen.it/nuclear/product.php?mod=V785

[GO4] GSI Analysis System Go4 http://www-win.gsi.de/go4/

[ROOT] Cern Data Analysis Framework ROOT http://root.cern.ch/

[RIO] http://fpsalmon.usc.es/genp/doc/DAQ/rio3_8064_datasheet.pdf

[Ant99] A. E. Antropov et. al, Nucl. Phys. Proc. Suppl. 78:416-421, 1999

[Kon08] N. A. Kondratiev, Investigation of fusion-fission reactions with position-sensitive MCP detectors, talk

[BLM15H] http://www.murata.com/products/catalog/pdf/c31e.pdf#BLM15H

[S66] http://www.minicircuits.com/pdfs/GALI-S66+.pdf

Danksagung

Ich möchte mich bei allen herzlich bedanken, die mich bei der Arbeit an meiner Bachelor-Thesis unterstützt haben.
Als erstes möchte ich besonders bei Herrn Dr. habil Hans-Jürgen Wollersheim für die Aufnahme in die Gamma-Spektroskopie-Gruppe an der GSI bedanken und dafür, dass er es mir ermöglicht hat, meine Bachelorthesis an der GSI zu schreiben.

Zweitens möchte ich mich bei Herrn Prof. Dr. Peter von Neumann-Cosel für die Universitäts-interne Betreuung bedanken und für seine Hilfe bei organisatorischen Fragen.

Dr. Plamen Boutachkov, Farheen Naqvi und Wolfgang König danke ich für die wunderbare Zusammenarbeit bei der Vorbereitung des UNILAC-Experiments und den ersten Einblick in den tatsächlichen Ablauf solcher Experimente.

Mein Dank geht auch an Ivan Kojouharov, Henning Schaffner und Wawrzyniec Prokopowicz für die Einführung in die Bedienung der Siliziumdetektoren, Elektronik und Datenaufnahme, sowie der Vakuumpumpen.

Weiterhin geht mein Dank an Prof. Alison Bruce, Dr. Stéphane Pietri, Robert Hoischen und Michael Bowry für einige Hilfe und vor allem moralische Unterstützung während der Vorbereitung der RISING-Experimente.

Vielen Dank an die gesamte Spektroskopie-Gruppe für die nette Arbeitsatmosphähre. Dank auch meine Zimmerkollegen Namita Goel, Tobies Engert, Tobias Habermann, Samuel Lago, Patrick Patchakui und Jennifer Ural für die gute Laune und gelegentliche Ablenkung.

Zum Schluss möchte ich mich noch bei meiner Familie und meinen Freunden bedanken, die mich in dieser Zeit unterstützt haben.

Erklärung zur Eigenständigkeit

Hiermit versichere ich, Eleonora Teresia Gregor, die vorliegende Bachelorarbeit ohne Hilfe Dritter und nur mit den angegebenen Quellen und Hilfsmitteln angefertigt zu haben. Alle Stellen, die aus Quellen entnommen wurden, sind als solche kenntlich gemacht worden. Diese Arbeit hat in gleicher oder ähnlicher Form noch in keiner Prüfungsbehörde vorgelegen.

Darmstadt, den 14.12.2009

Eleonora Teresia Gregor